**Characterization of Tropical Cyclone Intensity
Using Microwave Imagery**

THESIS

Amanda M. Nelson, Capt, USAF

AFIT-ENP-MS-19-M-087

**DEPARTMENT OF THE AIR FORCE
AIR UNIVERSITY**

AIR FORCE INSTITUTE OF TECHNOLOGY

Wright-Patterson Air Force Base, Ohio

AFIT-ENP-MS-19-M-087

CHARACTERIZATION OF TROPICAL CYCLONE

INTENSITY USING MICROWAVE IMAGERY

THESIS

Presented to the Faculty

Department of Engineering Physics

Graduate School of Engineering and Management

Air Force Institute of Technology

Air University

Air Education and Training Command

in Partial Fulfillment of the Requirements for the

Degree of Master of Science in Atmospheric Science

Amanda M. Nelson, B.S.

Capt, USAF

March 2019

CHARACTERIZATION OF TROPICAL CYCLONE

INTENSITY USING MICROWAVE IMAGERY

THESIS

Amanda M. Nelson, B.S.
Capt, USAF

Committee Membership:

Maj Omar A. Nava, Ph.D.
Chair

Matthew E. Kucas, M.S.
Member

Burcu Kosar, Ph.D.
Member

Robert D. Loper, Ph.D.
Member

AFIT-ENP-MS-19-M-087

Abstract

In the absence of wind speed data from aircraft reconnaissance of tropical cyclones (TCs), analysts rely on remote sensing tools to estimate TC intensity. For over 40 years, the Dvorak technique has been applied to estimate intensity using visible and infrared (IR) satellite imagery, but its accuracy is sometimes limited when the radiative effects of high clouds obscure the TC convective structure below. Microwave imagery highlights areas of precipitation and deep convection revealing different patterns than visible and IR imagery. This study explores application of machine learning algorithms to identify patterns in microwave imagery to infer storm intensity, particularly focusing on weaker storms where other analysis methods struggle. An analysis of 91 GHz Special Sensor Microwave Imager/Sensor imagery onboard various Defense Meteorological Satellite Program assets from February 2006 to 2017 is presented. Incorporating pattern recognition methods into the current analysis process at the Joint Typhoon Warning Center has the potential to significantly improve TC intensity estimates across all basins of responsibility.

Acknowledgements

First, I have to thank my husband for his relentless support and taking care of our daughter while I spent long days and nights working. Secondly, I would like to thank my daughter for always making me laugh and helping me keep everything in perspective. Their loving dedication has spurred me through sleepless nights and research missteps. I would not be where I am today without them.

I would also like to thank my parents and siblings for their love and words of encouragement over the past year and half, and the 28 years before. Specifically, my dad and sister for reading through this thesis and giving corrections and advice that improved the presentation of this research.

I could not have completed this without tireless assistance and guidance from my advisor. Throughout the process he has instructed and corrected me when I was heading in the wrong direction. I would also like to thank my committee members who took time out of their busy schedules to assist and advise me in their areas of expertise. Additionally, I would like to thank Capt Sean Zoufaly and Matt Kucas from JTWC for walking me through the operations at JTWC that allowed me to fully understand the need for this project.

Finally, I would like to thank my classmates for going through this journey with me. We had difficult classes and made wonderful memories along the way. I thank them for their friendship and support. I did not accomplish this alone and truly thank every person that has supported me along the way in their unique way.

Amanda M. Nelson

Table of Contents

List of Figures

List of Tables

List of Abbreviations

ADT Advanced Dvorak Technique

AMS American Meteorological Society

AMSR2 Advanced Microwave Scanning Radiometer 2

AMSR-E Advanced Microwave Scanning Radiometer for Earth Observing System

AMSU Advanced Microwave Sounding Unit

ARCHER Automated Rotational Center Hurricane Eye Retrieval

ATMS Advanced Technology Microwave Sounder

CIMSS Cooperative Institute for Meteorological Satellite Studies

CIRA Cooperative Institute for Research in the Atmosphere

DAV Deviation Angle Variance Technique

DMSP Defense Meteorological Satellite Program

DoD Department of Defense

DT Dvorak Technique

EM electromagnetic

FNMOC Fleet Numerical Meteorology and Oceanography Center

GMI GPM Microwave Imager

GPM Global Precipitation Measurement

IR infrared

JAXA Japan Aerospace Exploration Agency

JMA Japan Meteorological Agency

JTWC Joint Typhoon Warning Center

MATLAB Matrix Laboratory

NASA National Aeronautics and Space Administration

NESDIS National Environmental Satellite, Data, and Information Service

NHC National Hurricane Center

NOAA National Oceanic and Atmospheric Administration

NRL Naval Research Laboratory

PCT polarization corrected brightness temperature

RGB red, green, blue

RSMC Regional Specialized Meteorological Centre

SATCON Satellite Consensus

SCAMS Scanning Microwave Spectrometer

SSM/I Special Sensor Microwave/Imager

SSMIS Special Sensor Microwave Imager/Sounder

$\mathbf{T}_B$ brightness temperature

TC tropical cyclone

TCP Tropical Cyclone Programme

TMI TRMM Microwave Imager

TRMM Tropical Rainfall Measurement Mission

US United States

WMO World Meteorological Organization

WP Western North Pacific

I. Introduction

Tropical cyclones (TCs) cause significant damage to people, property, and resources totalling billions of dollars globally each year. As an example, the costliest year for the United States (US) was 2005 when TC damages reached 143.9 billion dollars (Blake et al., 2011). The US Department of Defense (DoD) aims to minimize TC impacts to DoD assets and personnel. Accurate TC forecasts are imperative for the DoD to guard their resources by initiating protective measures. The Joint Typhoon Warning Center (JTWC) is responsible for issuing TC forecasts and providing warning support for the DoD and other US government agencies across the Pacific and Indian Oceans. JTWC is manned by both Navy and Air Force military and civilian personnel.

Aircraft reconnaissance missions are frequently flown in the Atlantic Ocean to investigate TCs, particularly those that are expected to make landfall. Dropsondes are released to measure the wind speeds and surface pressure within the TC. However, the Atlantic is the only basin where aircraft reconnaissance missions are routinely flown through the storm center. When these observations are unavailable analysts rely on satellite remote sensing to track and estimate the intensity of TCs. Visible and infrared (IR) sensors aboard geostationary satellites are able to consistently observe TCs at a temporal resolution of up to 10 minutes. This allows near real-time tracking and a multitude of visible and IR imagery to analyze to estimate TC intensity.

The most widely used method to determine the intensity from satellite data is the Dvorak Technique (DT), which analyzes visible and IR imagery. However, there are other bands in the electromagnetic (EM) spectrum that are used to sense atmospheric phenomena. The microwave band provides additional information about TCs that cannot be captured by visible or IR sensors. Microwave radiation can pass through clouds unlike visible and IR, which means that middle and lower level features

beneath the high cloud layer can be sensed by microwave instruments. This allows the structure of a TC to be observed by a satellite orbiting Earth.

Currently, there is no universally accepted method to estimate intensity from microwave imagery. The objective of this research is to identify patterns in microwave imagery that relate to TC intensity, similar to how the DT relates visible and IR imagery to TC intensity. This research implements cluster analysis, a type of machine learning, to identify potential patterns.

Estimating TC intensity with microwave imagery or data gathered through microwave sensing is an active area of research. There have been a number of objective algorithms developed that utilize temperature sounding data from microwave sensors, some of which have been incorporated into operational TC forecasting centers (Ritchie et al., 2014). However, methods that analyze microwave imagery are less prevalent. Most, if not all, of the methods devised in the past decade apply computationally expensive algorithms to address the problem. None to our knowledge have applied the relatively simple cluster analysis to directly reveal patterns that correlate to intensity. There is one study by the Japan Meteorological Agency (JMA) that applies cluster analysis as a first step, but then goes on to apply a regression equation to determine the intensity (Sakuragi et al., 2014). Experienced analysts at JTWC have subjectively identified microwave imagery patterns related to various TC intensity ranges. These patterns are used as an analysis aid at JTWC to supplement the DT and other intensity estimation methods. An objective scientific backing to these patterns would bolster confidence in their use.

Perkins (2018) conducted initial research into identifying patterns in microwave imagery that relate to TC intensity, which this study builds upon. The background section will provide enough information on TCs and microwave remote sensing to establish the baseline knowledge needed to appreciate this research. However, more

emphasis was placed on describing cluster analysis since this was a new component of the research. For a more in-depth explanation of microwave remote sensing as related to TCs please reference Perkins (2018).

This chapter introduced the motivation and objective of this research while highlighting that this specific approach is new. Chapter II provides a brief review on TCs, the DT, microwave remote sensing, developments in intensity estimation since the DT, and cluster analysis. Chapter III details the methodology including data selection, image processing, and cluster analysis procedures. Chapter IV presents the results of multiple clustering trials and analyzes interesting patterns that emerged in the data. Lastly, Chapter V discusses potential impacts of this research, limitations, and future work ideas.

II. Background

2.1 Tropical Cyclones

TCs are warm core low pressure systems that form over warm tropical oceans around the globe (Chan and Kepert, 2010). TCs begin as areas of disorganized enhanced convection. If this area of enhanced convection develops a rotational circulation of a few hundred kilometers (km) it transitions to a tropical depression. Once the rotational circulation has developed the system is typically considered to be self-sustaining. Under favorable environmental conditions the tropical depression will intensify to tropical storm strength and eventually typhoon strength (or equivalent in other basins). As a TC reaches maturity the inner core becomes nearly axisymmetric. There is a relatively calm eye in the center with a typical diameter of 20-100 km. The eye is partly or fully surrounded by an intense ring of convection called the eyewall. Finally, spiral rainbands extend out from the center and rotate cyclonically around the eye (Chan and Kepert, 2010). The innermost area of a TC can be divided into the inner core and outer core. There are multiple definitions for the size of the inner and outer core. One from Weatherford and Gray (1988) defines the inner core as 0 - 1° latitude (0 - 111 km) and the outer core as 1°- 2.5° latitude (111 - 278 km).

There are seven TC formation areas, also referred to as basins; four in the Northern Hemisphere and three in the Southern Hemisphere. These basins are defined by the World Meteorological Organization (WMO) as the North Atlantic, Eastern North Pacific, Western North Pacific (WP), North Indian, Southwest Indian, Northwest Australian/Southeast Indian, and Northeast Australian/Southwest Pacific, illustrated in Figure 1. The WMO Tropical Cyclone Programme (TCP) is charged with establishing and managing regionally coordinated systems to minimize the loss of life and property caused by TCs. The seven TC Regional Specialized Meteorological

4
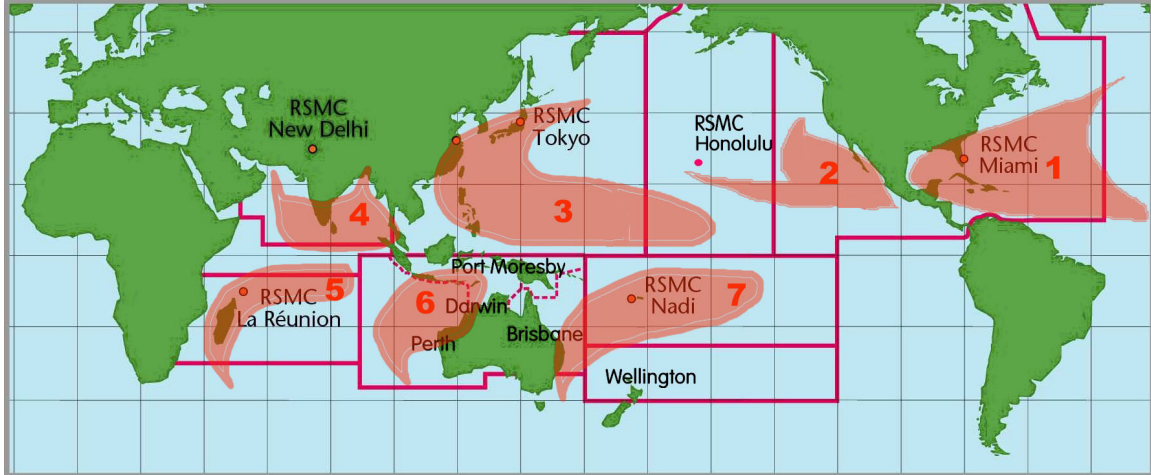
Figure 1. These are the TC basins as defined by World Meteorological Organization (2017): 1)North Atlantic, 2)Eastern North Pacific, 3)Western North Pacific, 4)North Indian, 5)Southwest Indian, 6)Northwest Australian/Southeast Indian, and 7)Northeast Australian/Southwest Pacific. Image from Hurricane Research Division (2014)

Centres (RSMCs), six of which are labeled in Figure 1, are responsible for advisories and bulletins for all TCs in their region (World Meteorological Organization, 2017).

The intensity of a TC is defined by the maximum wind speed and minimum sea level pressure of the storm. TC nomenclature depends on the basin and intensity of a storm, the various naming conventions are shown in Figure 2. However, the nomenclature listed for JTWC in Figure 2 is specific to the WP. The US National Hurricane Center (NHC) and Central Pacific Hurricane Center (CPHC) separate hurricanes into five categories based on the Saffir-Simpson Scale displayed in Table 1.

Table 1. The Saffir-Simpson Hurricane Wind Scale used by the US to categorize TCs.

Category	Wind Speed (kt)
1	64-82
2	83-95
3	96-112
4	113-136
5	137 or higher

MAXIMUM WIND (KNOTS)	SOUTHWEST INDIAN OCEAN	NORTH INDIAN OCEAN	WESTERN NORTH PACIFIC	S. PACIFIC/S.E. INDIAN OCEAN	NORTH ATLANTIC/ E. NORTH PACIFIC	JTWC AREAS OF RESPONSIBILITY	MAXIMUM WIND (KM/H)
10	Tropical Disturbance	Low Pressure Area	Tropical Depression	Tropical Depression	Tropical Depression	Tropical Depression	20
20		Depression					40
30	Trop. Depression	Deep Depression					60
40	Moderate Tropical Storm	Cyclonic Storm	Tropical Storm	Tropical Cyclone with Gale Force Winds	Tropical Storm	Tropical Storm	80
50	Severe Tropical Storm	Severe Cyclonic Storm	Severe Tropical Storm	Tropical Cyclone with Storm Force Winds			100
60							120
70	Tropical Cyclone	Very severe Cyclonic Storm	Typhoon	Tropical Cyclone with Hurricane Force Winds -or- Severe Tropical Cyclone	Hurricane	Typhoon	140
80							
90							160
100	Intense Tropical Cyclone						180
110							200
120	Very Intense Tropical Cyclone	Super Cyclonic Storm				Super Typhoon	220
130							240
140							260
	RA I	PANEL COUNTRIES	TYPHOON COMMITTEE	RA V	RA IV		

Figure 2. Nomenclature of TCs from World Meteorological Organization (2017). The JTWC nomenclature listed is specific to the Western North Pacific only.

2.2 Dvorak Technique

Satellite images have been used to determine TC intensity since the early 1960s. At that time only one satellite image was available per day. Satellite technology improved through the 1960s with the development of IR sensors and geostationary orbits. A satellite in geostationary orbit remains above the same point on Earth at all times so its field of view is constant. These improvements provided tropical meteorologists the ability to observe the evolution of TCs at a finer temporal resolution. They observed a relationship between TC development and the cloud patterns seen in satellite images. One of the most critical discoveries made during this period was that "cloud patterns of tropical cyclones evolve through recognizable stages as the intensity of

6

the cyclone changed" (Dvorak, 1984). The cloud pattern experiences periods when it is more and less defined during the development of a TC. Therefore, the intensity was difficult to determine if the satellite image was taken when the cloud pattern was less defined. It became clear that analysis procedures and rules would need to be developed. These procedures could then be used in conjunction with the cloud patterns to obtain accurate intensity estimates from satellite images (Dvorak, 1984).

The Dvorak TC intensity estimation technique was first developed in the early 1970s to fill this demand. Dvorak (1984) details the technique and provides forecaster tools for employing it. The technique was first used operationally early in the 1970s and underwent continuous improvements through the years. There are analysis techniques for both visible and IR data, which follow a similar series of steps illustrated in Figure 3 from Dvorak (1984).


```
STEP 1.  Locate cloud system center.

T-NUMBER ESTIMATE FROM              T-NUMBER ESTIMATE FROM
CLOUD FEATURE MEASUREMENT           PATTERN COMPARISON WITH MODEL

STEP 2.   Select pattern below (when    STEP 3.   "Central Cold Cover" (CCC)
          applicable).
          Analyze as instructed.        Determine the following:

STEP 2A.  "Curved band" pattern.        STEP 4.   Past 24-hour trend.

STEP 2B.  "Shear" pattern.              STEP 5.   Model expected T-number (MET).

STEP 2C.  "Eye" pattern.                STEP 6.   Pattern T-number.

STEP 2D.  "CDO" pattern.                STEPS 7, 8, and 9.   Determine final
                                                  T-number and CI-number using
STEP 2E.  "Embedded center" pattern.              rules.

                                        STEP 10.  Make 24-hour intensity
                                                  forecast using rules.
```

Figure 3. A simplified flow chart from Dvorak (1984) to determine TC intensity from visible/IR satellite imagery. ©American Meteorological Society

CI Number	MWS (Knots)	MSLP (Atlantic)	MSLP (NW Pacific)
1	25 K		
1.5	25 K		
2	30 K	1009 mb	1000 mb
2.5	35 K	1005 mb	997 mb
3	45 K	1000 mb	991 mb
3.5	55 K	994 mb	984 mb
4	65 K	987 mb	976 mb
4.5	77 K	979 mb	966 mb
5	90 K	970 mb	954 mb
5.5	102 K	960 mb	941 mb
6	115 K	948 mb	927 mb
6.5	127 K	935 mb	914 mb
7	140 K	921 mb	898 mb
7.5	155 K	906 mb	879 mb
8	170 K	890 mb	858 mb

Figure 4. The relationship between CI number (and T-number) and TC intensity as defined by Dvorak (1984). ©American Meteorological Society

However, Figure 3 is merely a simplified outline of the DT (reference Appendix A for a detailed flowchart). The output of the DT is a Tropical number (T-number) that results in the current intensity (CI) estimate of a TC. Figure 4 shows the table from Dvorak (1984) that defines this relationship for each CI number, the intensity is defined the same for the T-numbers. This method was developed over decades by observing and studying satellite imagery. However, it does not include an assessment of microwave imagery, which was not available until 1987. Due to the capabilities of microwave sensing there is a large amount of interest in incorporating microwave imagery into the intensity estimation process.

2.3 Microwave Remote Sensing

Satellite remote sensing of the earth and its atmosphere is possible because EM radiation is absorbed, reflected, scattered and emitted by the earth system. The re-

sponse of an EM wave when encountering a particulate is dependent on the wavelength of the incident radiation in addition to the size, shape, and molecular properties of the atmospheric constituent it interacts with. Atmospheric phenomena can be observed by exploiting different bands within the EM spectrum. The transparency of Earth's atmosphere varies depending on which band of the EM spectrum it is viewed in and the amount of water vapor present in the atmosphere. The three bands most commonly used to observe meteorological phenomena are the visible, IR, and microwave bands (Petty, 2006).

A dry atmosphere is almost completely transparent in the visible band. However, clouds are highly reflective of incoming solar radiation, therefore they are not transparent. Within the IR and microwave bands there are ranges of wavelengths where a cloud-free atmosphere is fairly transparent, these are called spectral windows. However, even within a spectral window in the IR band clouds are not transparent because IR radiation emitted by Earth's surface does not pass through clouds. Therefore, neither visible nor IR sensors can be used to observe conditions below or within clouds. On the other hand, clouds are semi-transparent in the microwave band allowing structure beneath cloud tops to be visible (Petty, 2006).

Water vapor and oxygen are particularly strong absorbers and emitters at certain wavelengths in the microwave band, Figure 5 from Petty (2006) shows these absorption bands. Outside of the two oxygen absorption bands at 60 and 118 GHz the dry atmosphere is nearly transparent. However, once water vapor is included transmittance through the atmosphere decreases as the frequency increases, note the solid line representing a tropical climate with high water vapor content in Figure 5.

Spatial resolution decreases with microwave sensors as compared to visible or IR because wavelengths are longer in the microwave band. Therefore, microwave sensors are flown on satellites in low earth orbit to improve the resolution. However, this

Zenith Microwave Transmittance
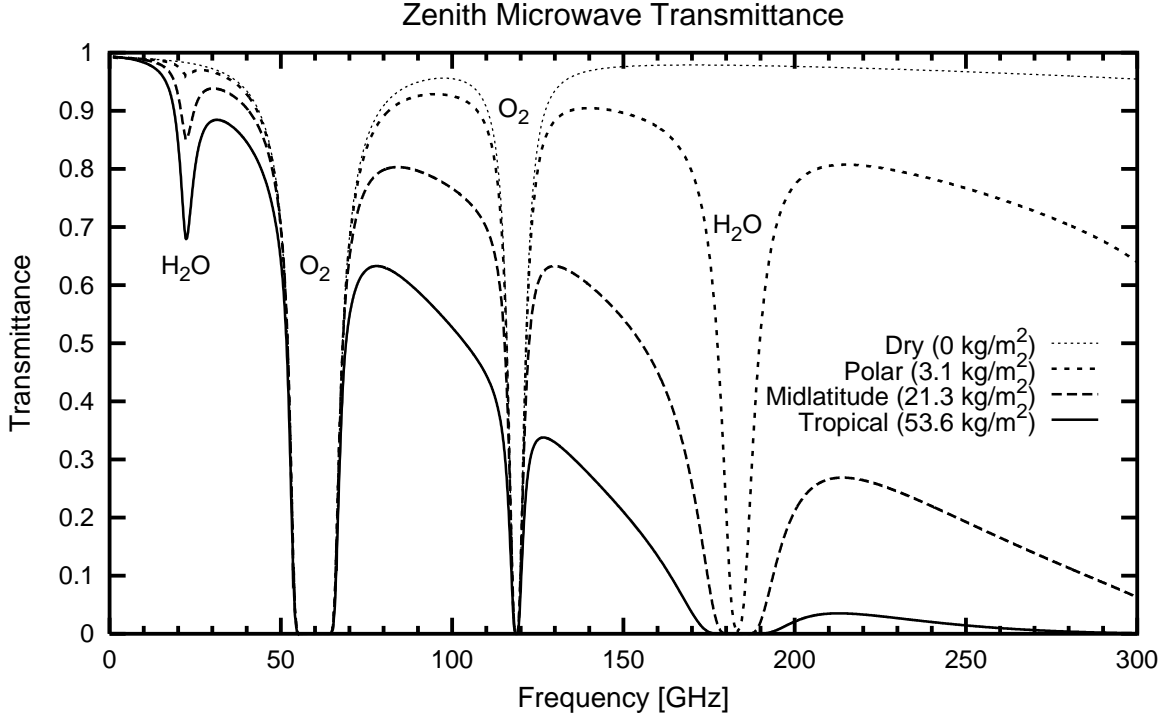
Figure 5. Zenith microwave transmittance of the cloud-free full-atmosphere. Absorption bands for H_2O and O_2 are highlighted. The H_2O effect varies with the average water vapor content, therefore transmission in dry air and three different air mass types (defined by water vapor content) are plotted (Petty, 2006). Used with permission.

orbit only allows each area on the earth to be observed twice a day. Furthermore, because there are gaps between each pass of a polar orbiter and TCs move quickly at times there are days where there may only be one or no images of a TC.

Different microwave frequencies are used to observe various properties of the TC. Low frequencies are able to observe information near the earth's surface due to the high transmittance, whereas higher frequencies sense meteorological parameters higher in the atmosphere. Transmittance through an atmosphere containing water vapor has local minima at 22 and 183 GHz and local maxima near 37 and 85 GHz.

Absorption bands are utilized when sounding the atmosphere. This technique exploits the sharp transition in absorptive properties over a short wavelength range. The main TC imaging channels are 37 GHz and from 85-91 GHz where maximal transmittance occurs. The 85-91 GHz imager channels are used to view the structure

10

of a TC including the rainbands and eyewall (Hawkins et al., 2008). This is possible because ice scatters microwave radiation in the 85-91 GHz channel which results in an "ice-scattering signature" (Cecil and Zipser, 1999). Ice indicates an area of deep convection highlighting the structure of a TC. Therefore, the frequencies between 85 GHz and 91 GHz are useful for investigating TC intensity.

The information output by a microwave imager is brightness temperature (T_B). T_B is not the physical temperature of the surface that radiation is emitted or scattered from. Rather, T_B is related to both the physical temperature at which the radiation was emitted and the particulates the radiation encounters prior to reaching the sensor (Petty, 2006). Ice scattering microwave radiation in the eyewall and rainbands results in lower T_B in these areas (Cecil and Zipser, 1999). Whereas, area covered by non-precipitating clouds will sense the microwave radiation emitted by the ocean surface which is relatively warm and displays as a warmer T_B. For instance a large well-developed eye will show up as a warmer T_B circle at the center of the TC.

2.3.1 Microwave Remote Sensing Instruments

The first microwave radiometer that measured radiation emitted and reflected from the earth was launched by the Soviet Union in September 1968 aboard Cosmos 243 (Gorbunov and Kutuza, 2018). The first scanning radiometer, which was important for furthering TC research, was aboard Nimbus 5, launched in 1972. Microwave radiometers are used to sense many meteorological parameters including temperature, moisture, and liquid water content. Additionally, wind speeds can be inferred over the ocean based on wave roughness (Kidder, 1978) However, this research exclusively analyzes microwave imagery therefore only imagers will be discussed from here on.

The first microwave imager was the Special Sensor Microwave/Imager (SSM/I) launched on the Defense Meteorological Satellite Program (DMSP) F-8 polar orbit-

ing satellite on 19 June 1987 (Hollinger, 1990). The follow-on to SSM/I was the Special Sensor Microwave Imager/Sounder (SSMIS) launched on DMSP F-16 on 18 Oct 2003 (Kunkee et al., 2008). Other microwave imagers include the Advanced Microwave Scanning Radiometer for Earth Observing System (AMSR-E), Advanced Microwave Scanning Radiometer 2 (AMSR2), Tropical Rainfall Measurement Mission (TRMM) Microwave Imager (TMI), and most recently Global Precipitation Measurement (GPM) Microwave Imager (GMI). TMI was launched aboard TRMM in 1997 as a joint venture between National Aeronautics and Space Administration (NASA) and Japan Aerospace Exploration Agency (JAXA). Unlike DMSP satellites, TRMM was not a polar orbiting satellite though it was still in a low earth orbit (Hou et al., 2014). The primary mission of TRMM was to provide precipitation estimates over the tropics. Therefore, it utilized a circular, non-sun-synchronous orbit with an inclination of 35° to the equator to maximize time spent over the tropics (NASA, b). TMI had a spatial resolution of 7 km x 5 km in the 85.5 GHz channel (Lee et al., 2002). TRMM ended its mission in April 2015 after depleting its fuel supply (Blumenfeld, 2015). Prior to the completion of TRMM's mission the GPM Core Observatory carrying GMI launched in February 2014. Its orbit was slightly different with an inclination of 65° to the equator, which extended its field of view to capture information over the midlatitudes in addition to the tropics (NASA, a). The spatial resolution of GMI in the 89 GHz band is 4.4 km x 7.3 km (Hou et al., 2014), similar to that of TMI. AMSR-E was in operation from June 2002 to October 2011 aboard the NASA Aqua satellite. Due to a mechanical failure AMSR-E ceased operations in October 2011. However, AMSR2 began operating in May 2012 on the JAXA Global Change Observation Mission 1st-Water satellite, essentially replacing AMSR-E. Both sensors were aboard polar orbiting satellites and had spatial resolutions in the 89 GHz band of 5 km x 3 km and 6 km x 4 km, respectively (Du et al., 2014).
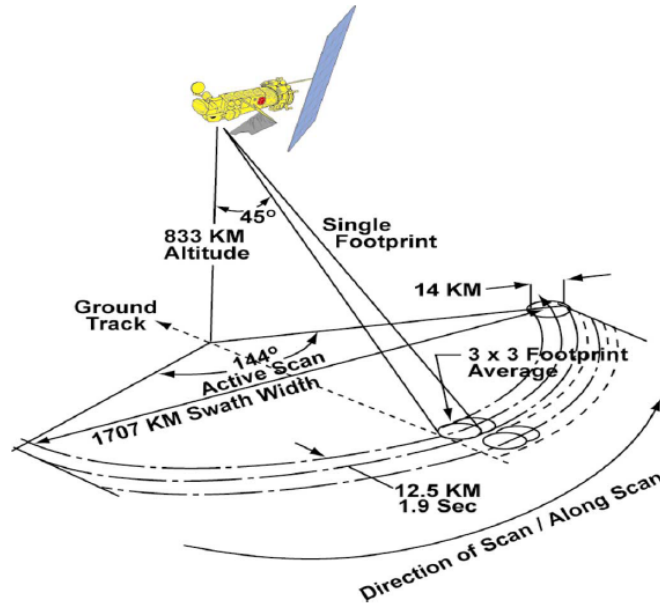
Figure 6. The SSMIS scan geometry from Kunkee et al. (2008).

2.3.2 Special Sensor Microwave Imager/Sounder (SSMIS)

The SSM/I has a swath width of 1,400 km and spatial resolution of 12.5 km in the 85.5 GHz channel (Hollinger, 1990). There were changes with the upgrade to SSMIS. The frequency of the channel of interest was changed from 85.5 GHz to 91 Ghz to reduce the complexity of the hardware. The conical scanning geometry and spatial resolution remained the same, but the swath width increased to 1,707 km (Kunkee et al., 2008). Figure 6 illustrates the scanning geometry for SSMIS.

The change from 85.5 GHz with SSM/I to 91 GHz with SSMIS affected the T_B display because of how each channel responds to frozen hydrometeors. There is increased scattering by frozen hydrometeors at 91 GHz as compared to 85.5 GHz resulting in lower brightness temperatures. Therefore, areas of convection are highlighted better with SSMIS. Additionally, the increase in swath width allows more TCs to be sensed by increasing the spatial coverage (Hawkins et al., 2008). Another advantage of SSMIS is that it is flying on three satellites: F16, F17, and F18.

2.4 Previous Research

2.4.1 Intensity Estimation Techniques

Since the DT there have been many other intensity estimation methods developed that use remotely sensed data. Some of these techniques have built upon the DT such as the Advanced Dvorak Technique (ADT), while others aim to be used in conjunction with the DT. Providing an exhaustive list of these methods is outside the scope of this research. However, prominent techniques and those most relevant to this thesis will be briefly introduced in this section.

2.4.1.1 Using Data from Microwave Sensors

The first microwave sensor used to infer TC intensity was the Scanning Microwave Spectrometer (SCAMS) aboard Nimbus 6, launched in 1975. Kidder (1978) proposed a method that deduced the central pressure of a TC from warm temperature anomalies in the upper troposphere. The outer surface wind speeds were calculated by assuming gradient balance and estimating the surface pressure gradient. There have been numerous studies since Kidder (1978) that attempt to determine TC intensity from microwave sounding data. This has led to five microwave sounder-based intensity estimation techniques that are routinely used in operational settings (Ritchie et al., 2014). Three of these methods are derived from algorithms that utilize data from the Advanced Microwave Sounding Unit (AMSU) instrument. These were developed by Cooperative Institute for Meteorological Satellite Studies (CIMSS), JMA, and Cooperative Institute for Research in the Atmosphere (CIRA)/National Environmental Satellite, Data, and Information Service (NESDIS). The fourth and fifth are produced by CIMSS and use data from SSMIS and Advanced Technology Microwave Sounder (ATMS), respectively, in their algorithms (Herndon and Velden, 2016).

14

Once satellite-based microwave imagery became available in 1987 numerous studies were conducted that attempted to relate the T_B to TC intensity. Although there were a few notable studies prior to it, Cecil and Zipser (1999) is often cited as landmark research for relating microwave T_B to TC intensity. Cecil and Zipser (1999) found high correlations between the 85 GHz mean polarization corrected brightness temperature (PCT), which was a proxy for updraft strength and precipitation intensity, and both current and 24-hour intensity.

Another development spurred by microwave imagery was an objective method to determine the TC center. It can be hard to identify the TC center on visible or IR imagery if an eye has not yet developed or the eye is covered by clouds. Wimmers and Velden (2010) designed an objective algorithm, Automated Rotational Center Hurricane Eye Retrieval (ARCHER), that ingests 85-92 GHz microwave imagery to determine the rotational center of a TC. There have been improvements to the initial algorithm. Wimmers and Velden (2016) details the improvements to the algorithm, which is now called ARCHER-2. ARCHER-2 ingests more data than the original version, now including visible and IR imagery from geostationary satellites in addition to scatterometer data and 37 GHz microwave imagery. Furthermore, it now provides an expected error score that tells the user how reliable the center fix provided was.

2.4.1.2 Using Data from Infrared and Visible Sensors

Perhaps the most prominent objective intensity estimation technique is the ADT, documented by Olander and Velden (2007). The ADT is a culmination of many research projects conducted by the University of Wisconsin-Madison's CIMSS. This research includes the Objective Dvorak Technique and Advanced Objective Dvorak Technique. The original goal of designing an objective DT was to mimic the original DT closely and merely automate the process to increase its objectivity. However, as

research into TC intensity has increased statistical evaluation of the technique led to some deviation from the original DT. The ADT algorithm is run operationally at the National Oceanic and Atmospheric Administration (NOAA)/NESDIS Satellite Analysis Branch and is used by JTWC, NHC, and other forecast centers (Ritchie et al., 2014).

An effort to combine the aforementioned techniques is underway at CIMSS. Satellite Consensus (SATCON) combines objective estimates from the ADT, the ATMS sounder algorithm from CIMSS and CIRA, and the SSMIS and AMSU sounder algorithms from CIMSS to determine the best intensity estimation (CIMSS, 2019). The SATCON algorithm performs better than each member individually and acts as an ensemble of objective intensity estimation techniques (Velden and Herndon, 2014).

2.4.1.3 Techniques that Apply Machine Learning

Recently machine learning has been utilized to address the difficult problem of estimating TC intensity. Pradhan et al. (2018) designed a deep convolutional neural network to categorize TCs by intensity using image recognition. The intensity categories were set using the Saffir-Simpson Hurricane Wind Scale. Estimating intensity from an image alone is a difficult problem to solve. The techniques discussed up to this point have involved significant image pre-processing and domain knowledge to choose the information that was fed into the estimation algorithms. However, convolutional neural networks are very good at recognizing images, which inspired this cutting-edge research.

The DT is built upon the idea that TCs have similar patterns when they are of a similar intensity, which supports the potential of Pradhan et al. (2018). Instead of relying on analysts to identify important features the algorithm steps through layers generating feature maps and selecting critical features from within these maps. This

16

method showed skill in identifying the correct categories as it learns from its mistakes and continually improves. This is a very significant development but is currently only applied to IR imagery. Furthermore, it requires significant computing power to train the initial algorithm as deep learning is a highly sophisticated technique.

Bankert and Cossuth (2016) looks specifically at determining TC intensity from microwave imagery. This research uses machine learning algorithms to select features within microwave images that are most indicative of intensity. While Bankert and Cossuth (2016) focuses on microwave imagery as opposed to sounding data the objective of the study is not to identify patterns that relate to intensity. Furthermore, the feature selection algorithms are likely still computationally expensive, albeit less so than Pradhan et al. (2018).

A less computationally intensive form of machine learning is cluster analysis. Clustering has been applied to TC tracks with the intent of determining any inter-annual variability in tracks due to large scale teleconnections. There are a number of studies that have explored this including Ramsay et al. (2012), Daloz et al. (2015), and Kim and Seo (2016). However, cluster analysis has rarely been applied to the problem of intensity estimation.

Only one research study applying cluster analysis to estimate TC intensity from microwave imagery was uncovered. Sakuragi et al. (2014) details an objective TC intensity estimation method developed by JMA. This method uses T_B information from five channels of the TMI, including the 85 GHz channel. The TC is divided into sections that are dependent on the direction of the storm motion. The mean, minimum, maximum, and ratio of pixels exceeding a defined T_B threshold were calculated for each section. This was done for each channel used of each polarization yielding a final 457 variables to be used for cluster analysis.

Sakuragi et al. (2014) applied k-means cluster analysis to the dataset separating the data into ten clusters. Once each cluster was created regression analysis was applied to each cluster to define a regression equation to relate five to seven of the original 457 variables to the maximum wind speed. The initial clusters were created from data from 1998-2008 then validation was accomplished on TCs from 2009-2012. During validation the images were once again clustered into 10 clusters using k-means then the regression equation determined from the 1998-2008 data was applied to see what the maximum wind speed was. This result was then compared to the best track maximum wind speed for analysis. Their results showed a bias near 0 m/s and a root-mean squared error of 6.26 m/s, which they note is comparable to the accuracy of the DT. While TMI data was available this method was used by the RSMC Tokyo-Typhoon Center as supplementary information to the DT.

2.4.2 Research this Thesis Directly Builds On

Perkins (2018) provided the proof of concept for this research wherein microwave imagery from four sensors was analyzed. The images were separated by intensity using Saffir-Simpson Scale categories. Then images in each intensity bin were composited together. Each intensity bin showed a different pattern with higher intensities containing more defined structure. However, since the images were not separated into like images the composite resulted in muddled patterns that were not representative of the entire intensity bin. This is where this research begins its focus. Cluster analysis is applied to the images, separated by intensity, to pick out common patterns that could subjectively signify a certain intensity. JTWC has a binder of microwave patterns that have been subjectively identified by experienced analysts to correspond to certain intensity ranges. Satellite analysts and forecasters refer to the images in this binder to identify patterns that resemble a current TC microwave satellite im-

age to estimate the current intensity based on the closest visual match. While this method has proven beneficial to the JTWC forecast process, it is highly unstructured and informal. This supports both the feasibility and necessity of this study.

2.5 Cluster Analysis

The primary objective of a machine learning algorithm is to learn from training data in order to assess unseen test data by performing various predefined tasks on the data provided. Machine learning problems are typically broken into supervised and unsupervised learning. Supervised learning, routinely called classification, assesses labelled data. Conversely, unsupervised learning involves only unlabeled data and can ultimately lead to the discovery of hidden patterns in data (Jain, 2010).

Cluster analysis is a type of unsupervised learning. The purpose of clustering data is to reveal the natural grouping of a set of objects. For instance, given some representation of n objects find k groups based on a similarity measure where the intra-group similarity is high and similarity between groups is low. Although humans are adept at recognizing patterns in two or three dimensions, clustering algorithms must be employed to pick out clusters from high-dimensional data (Jain, 2010).

Clustering algorithms can be separated into two main groups: hierarchical and partitional. Hierarchical clustering can further be subdivided into agglomerative or divisive. Agglomerative hierarchical clustering begins with each object in its own cluster, then matches them based on similarity, starting with the most similar two objects. In contrast, divisive hierarchical clustering starts with all objects in one cluster then breaks a cluster into two at each step until each object is in its own cluster. Unlike hierarchical clustering, partitional clustering algorithms find all clusters at the same time rather than in steps. One of the most widely-used partitional clustering algorithms is k-means due to its simplicity and efficiency (Jain, 2010).

2.5.1 K-means Clustering

K-means was first discovered in 1956 and was found by four different research teams independently across scientific fields between 1956-1967. K-means clusters data by minimizing the squared error between the mean of the cluster and the points in the cluster. Figure 7 displays the steps taken by k-means to identify clusters. Although the algorithm appears quite simple there are important limitations that must be taken into consideration.

There are three user defined parameters in k-means: the number of clusters (k), the initial clusters created, and the distance metric. The final clusters output by k-means are affected by the cluster initialization because k-means converges to local minima. One method used to try to correct this is to replicate k-means with different initializations and choose the run with the smallest squared error. However, Steinley (2003) noted that for a medium-sized dataset with 200 objects and 8 features there could be thousands of unique local optima. Therefore, Steinley (2003) advises completing many thousand random initializations and choosing the one with the smallest sum of squared error. However, this is viewed as a clumsy approach that may still provide a sub-optimal result. Although this is a serious limitation of k-means, Jain (2010) states that the most critical choice is the value of k.

There is no formula to objectively determine the correct number of clusters. Typically, k-means is run for multiple values of k and the results are reviewed by an expert in that field to determine what the best k for the dataset is. However, there are many methods that can be applied to search for the optimal k. For example, the elbow method is one well-known technique. An error measure is plotted which decreases as k increases. Sometimes there is a clear point at which the error decreases less rapidly, this k is the elbow and is considered the optimal k (Tibshirani et al., 2001). There are other methods that could be discussed, but they are outside the
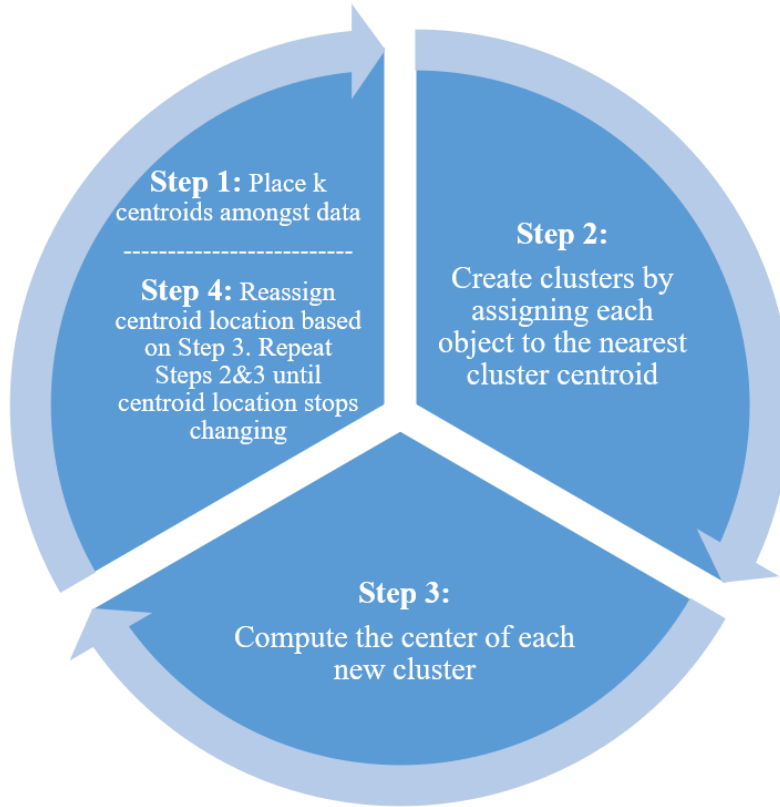
Figure 7. The general steps taken during k-means cluster analysis.

scope of this project as there is no standard approach. Next, hierarchical clustering will be described, which is another widely used clustering algorithm (Jain, 2010).

2.5.2 Hierarchical Clustering

Agglomerative hierarchical clustering is the most commonly used type of hierarchical clustering. There are three user defined parameters within hierarchical clustering: the distance metric, the linkage method, and where the tree is cut to create clusters. The steps of hierarchical cluster analysis are laid out in Figure 8.

Each step in Figure 8 represents a decision point that must be made by the user. Within Matrix Laboratory (MATLAB), a programming platform popular in engineering and science, there are twelve built-in distance metrics or users can define

Create Similarity Matrix	• Compute similarity between each pair of objects with user-defined distance metric
	• Similarity matrix constructed from computations
Create Hierarchical Tree	• Link pairs of objects together, first linking the most similar objects
	• Once a pair is linked the new similarity matrix is computed with either single, average, or complete linkage
Decide where to Cut Tree	• Cut tree by specifying arbitrary maximum clusters or using the inconsistency coefficient to determine natural breaks in the data

Figure 8. The general steps taken during hierarchical cluster analysis.

their own. Once the distance metric is chosen a similarity matrix is created by calculating the distance between each pair of objects using features provided to the computer. After the s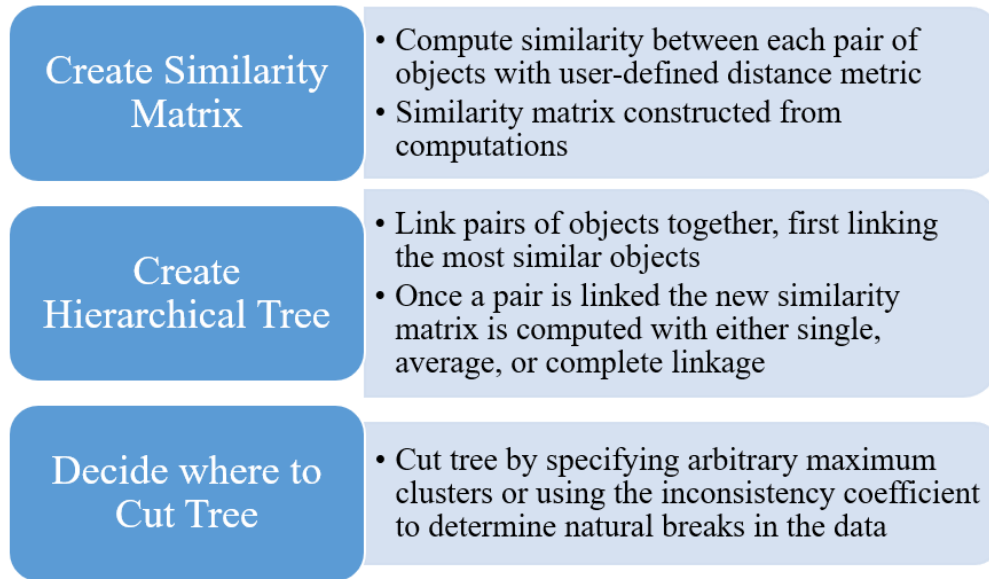imilarity matrix is created the objects are grouped based on linkage method. The most common linkage methods are single linkage and complete linkage (Jain, 2010). When a pair is joined a new similarity matrix is created with the pair acting as a new object. For single linkage the smallest distance of the two is used, whereas in complete linkage the largest distance is used to recalculate the distance between the now "paired" object and all other objects. The output of linking the objects based on similarity is a matrix, where each row represents a step and contains information about the pair of objects that was combined. Once the tree is created the user can choose to cut it by specifying arbitrary maximum number of clusters or by finding natural divisions in the data through the inconsistency coefficient. The inconsistency coefficient compares the similarity of a pair against all others at that same step in the hierarchy to determine natural breaks in the data (The MathWorks Inc, 2015).

Hierarchical clustering is convenient because the clusters created can be easily viewed. The best way to view them is by forming a dendrogram from the output from Step 2. This allows the user to visualize their clusters and assess natural groupings based on the shape of the divisions. However, this is not the only way to view the data. Once clusters are identified by an algorithm it is useful to run an analysis to determine if objects were placed in the right cluster. One popular tool to do this is the silhouette plot (The MathWorks Inc, 2015).

2.5.3 Silhouette Plot

Rousseeuw (1987) proposed a graphical display of clusters produced by clustering algorithms called silhouettes. The purpose is to determine how likely an object is in the correct cluster. Figure 9 contains example objects divided into clusters to accompany Equation 1, which defines how the silhouette value is calculated for each object:

$$s(i) = \frac{b(i) - a(i)}{max(a(i), b(i))}.$$

(1)

In Equation 1 $a(i)$ is the average dissimilarity of i to all other objects of A, in Figure 9 this is the average length of all lines in A. In order to calculate $b(i)$ Rousseeuw (1987) first defines $d(i, C)$ as the average dissimilarity of i to all object of C, in Figure 9 this is the average length of all lines going from i to C. Next, d is calculated for every cluster that is not A. Then, the smallest average distance is selected as b(i), such that $b(i) = \underset{C \neq A}{minimum}\, d(i, C)$.
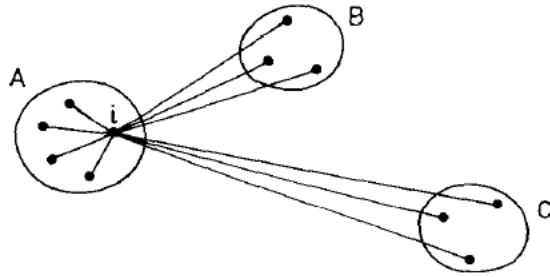
Figure 9. An illustration of the components used to compute $s(i)$ in Equation 1 from Rousseeuw (1987). Used with permission.

The silhouette value will always fall between -1 and 1. A silhouette value of 1 means the object has the highest likelihood of belonging in that cluster, whereas a value of -1 means the object has the lowest likelihood of belonging in that cluster. A value of 0 is neutral, not indicating either way if the object belongs in that cluster.

III. Methodology

3.1 Data Selection

The microwave images analyzed in this research were originally-generated by Naval Research Laboratory (NRL) and Fleet Numerical Meteorology and Oceanography Center (FNMOC) and provided by JTWC through their on-site secure server. Receiving the data directly from JTWC was preferable because there were no country borders, latitude, or longitude lines overlaid on the images. JTWC creates best track files for each storm during the post-storm review. All available data is reviewed by three people with the benefit of hindsight and time to complete an intensive review. The final product is the best estimate of reality in the absence of aircraft observations. JTWC has access to data from five microwave imagers and two microwave sounders, from which imagery is derived, across five basins. Yet, to minimize the amount of variability in the data analyzed this research focuses on the WP basin using 91 GHz microwave imagery from SSMIS.

The WP basin was chosen because it has the highest frequency of TCs, approximately 30% of the global total (World Meteorological Organization, 2017). Additionally, there is a limited number of large islands in the basin. This is desirable because TC structure is affected when storms encounter land. Gray (1968) noted that TCs can form in the WP in any month but the highest concentration occurs during boreal summer. The borders of the WP basin are the 180° longitude line and the Asian coastline with the area of maximum TC intensification occurring between 130°E and 150°E (Gray, 1968).

SSMIS was selected as the preferred sensor because there is more data available for it. SSMIS has flown on three DMSP satellites, whereas other imagers introduced in Section 2.3 have only flown on one satellite, with the exception of SSM/I. The

25

final imagery was selected with strict criteria to produce optimal results, which will be detailed in Section 3.3.

3.2 Image Processing

TCs are tracked by JTWC using an annual cyclone number. The TC numbers start at 01 for the first storm of the calendar year, then increase by 1 for each subsequent storm in that specific basin. The best track data compiled by JTWC is stored in a single document per storm, labeled with a 'b' for best track, the basin, TC number, and year, i.e. 'bwp052009.txt'. Information about the TC is recorded every 6 hours at 00Z, 06Z, 12Z, and 18Z. Up to 35 pieces of data related to the TC are recorded at each time step. The best track data includes the date, time, latitude and longitude of the storm center, maximum sustained wind speed, and minimum sea level pressure among other storm properties. Similar data are stored within the filename of the imagery obtained from JTWC. Figure 10 shows an example filename and highlights the data contained within it.

The images received from JTWC were not storm-centered. Additionally, some maximum wind speeds were revised in the best track data causing the wind speed encoded in some files' names to be incorrect. Matthew Kucas, JTWC Technical Services Team Chief, provided the script to process the images so they could be used in this research. Figure 11 outlines the image processing steps.
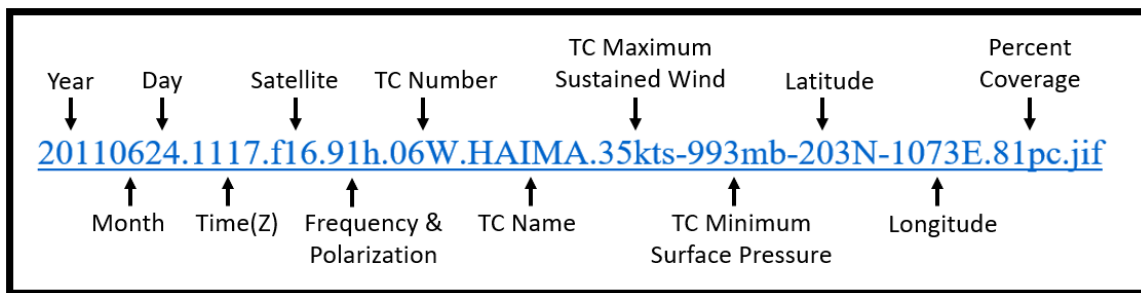

Figure 10. Example of the file naming convention for the images provided by JTWC.

26

Download Files
- Download best track files from JTWC webpage
- Dowload SSMI/S imagery from JTWC PZAL server using wget

Import Data
- Create directory of all images for each storm
- Loop through directory adjusting one image at a time
- Store information from best track file and image filename as variables

Compute Best Estimates
- Interpolate best estimate of intensity and location at image time
- Calculate vector between current image center and new TC center based on associated best track data
- Crop image based on new best track TC center

Save Revised Images
- Only save images that are not near land
- Save image with the intensity and location estimates (derived from best track data) in filename
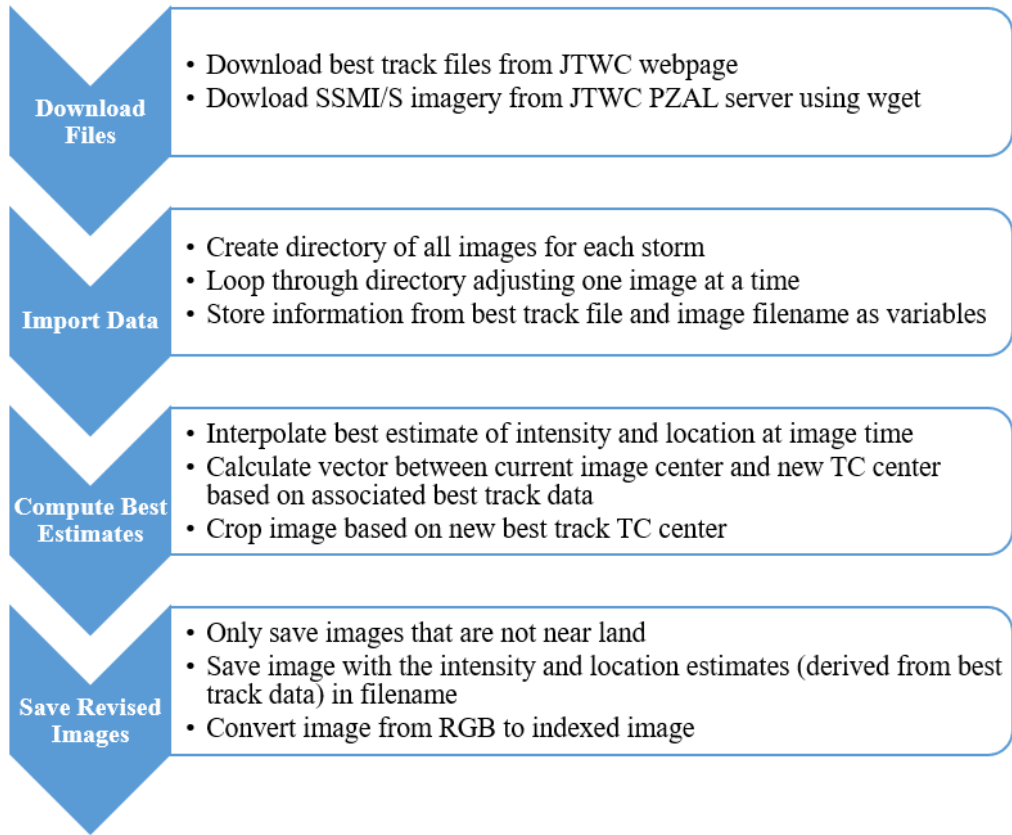- Convert image from RGB to indexed image

Figure 11. Flowchart outlining the steps taken during image processing.

All scripts were created and run through MATLAB. The images were stored as a matrix, moving through the dataset one storm at a time. Next, the best track file for that storm was imported and scanned. The TC number, date/time of observation, latitude and longitude of the center, storm development level, maximum wind speed and minimum central pressure were stored as variables. Next, the date, time, and latitude/longitude at the center of the image is extracted from the image filename and stored.

The image time was used in conjunction with the best track data to interpolate the center location and maximum wind speed at the time of the image. Next, the image is recentered on the interpolated best track location by determining the distance and direction between the original image center location and the new interpolated best

27

track center location. The image is then cropped based on the new center position to a 401x401 pixel image, with the interpolated center location at pixel [201,201]. Finally, if the entire bounds of the recentered image fell within the bounds of the original image it was saved with the interpolated best track wind speed and center location in the new filename for future reference.

The recentered images were initially saved as red, green, blue (RGB) images, meaning each pixel had a red, green, and blue value. In order to run cluster analysis on the images each pixel could only have one reference value. The RGB images were converted into indexed images so that each pixel had only one value associated with it. When the indexed image is displayed with the original color map the microwave T_B correspond directly to the new pixel values, illustrated in Figure 12. Before beginning cluster analysis the images were refined based on requirements of the clustering algorithm and experiment-imposed restrictions.
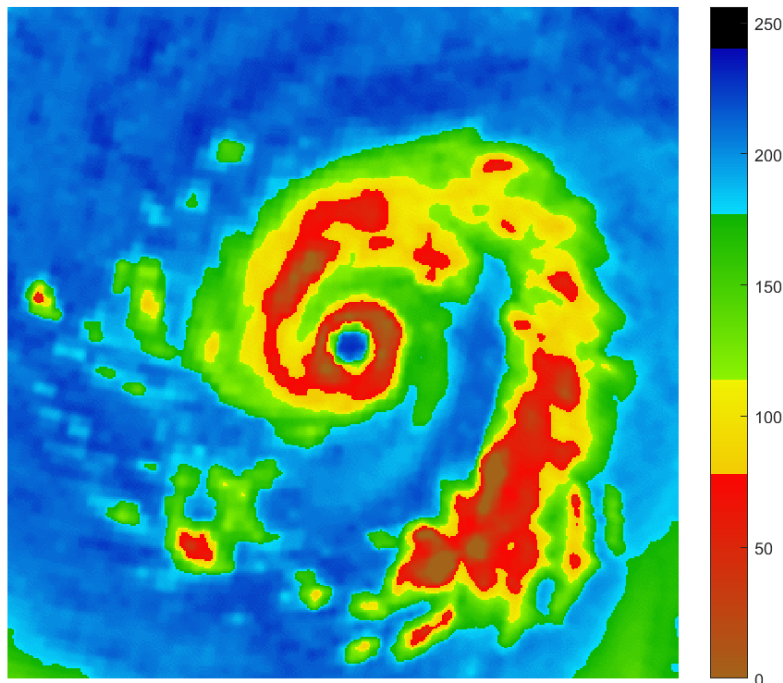

Figure 12. Typhoon Dolphin (2015) - Example of an indexed image, note the color bar on the right indicating that the pixel values are related to the brightness temperatures. The image is 401x401 pixels which equates to approximately 800 km x 800 km.

3.3 Image Selection Criteria

In order to optimize the data analyzed three general restrictions were imposed on the images used, shown in Table 2. These will be expanded upon in this section.

Table 2. Image selection criteria

Coverage	No images with data missing
Temporal	There cannot be two images within a one-hour time-span
Location	No TCs over land (see Table 3)

3.3.1 Automated Criteria

Two restrictions were placed within the initial image processing code. First, the percent coverage was limited to greater than or equal to 80%. Initially, the threshold was set at greater than or equal to 70%, but all images with less than 80% coverage resulted in final images with missing data. For this initial study, this methodology does not incorporate images with missing data. Therefore, the cutoff was set at 80% to avoid tediously deleting unusable images later in the process.

Secondly, no TCs over land were included in the dataset, due to structural changes that occur when TCs encounter land (Stenger, 2013). This was accomplished by setting longitude cutoffs based on latitude ranges. Any TC with a center west of the longitude cutoff was not included. Figure 13 illustrates these cutoffs that are listed in Table 3.

Table 3. The location criteria used to eliminate images of TCs over land.

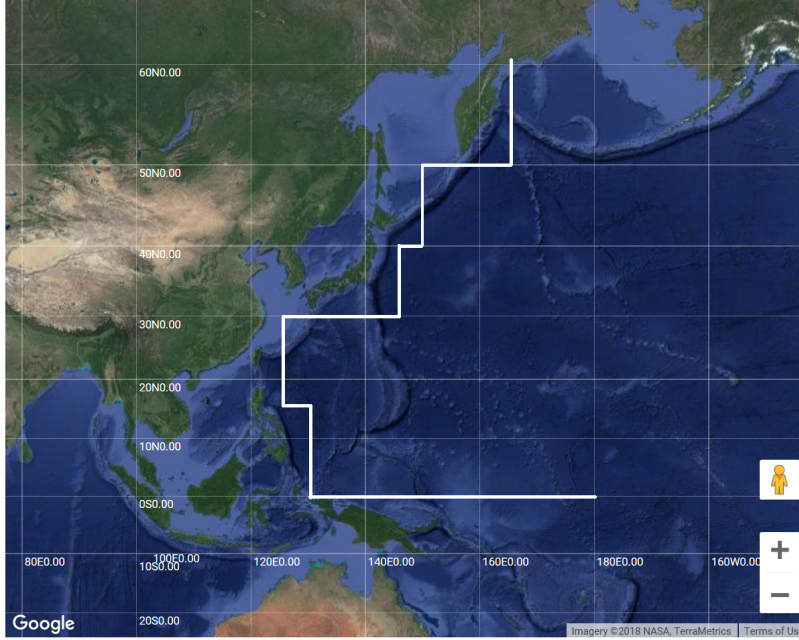| Latitude Range	Longitude Cutoff
0 - 15°N	130°E
15.1°N - 30°N	125°E
30.1°N - 40°N	145°E
40.1°N - 50°N	150°E
50.1°N - Max Latitude	165°E

Figure 13. Map of the cutoff values listed in Table 3. Any TC center that was west of the white line was discarded, the equator is also highlighted. Underlying imagery from ©2018 NASA TerraMetrics, Google.

3.3.2 Manually Executed Criteria

Once the images were processed, they were manually examined to ensure the highest quality. Any images that were missing data, even a tiny fraction as illustrated in Figure 14, were discarded. Additionally, when two images were within an hour or less of each other one of the images was discarded. This was done because the structures were so similar that it was akin to having two of the same images, which would weight that pattern over others. Table 4 displays the number of images originally received from JTWC and the number remaining after each restriction was imposed.

Table 4. The number of images available for analysis after each restriction was imposed.

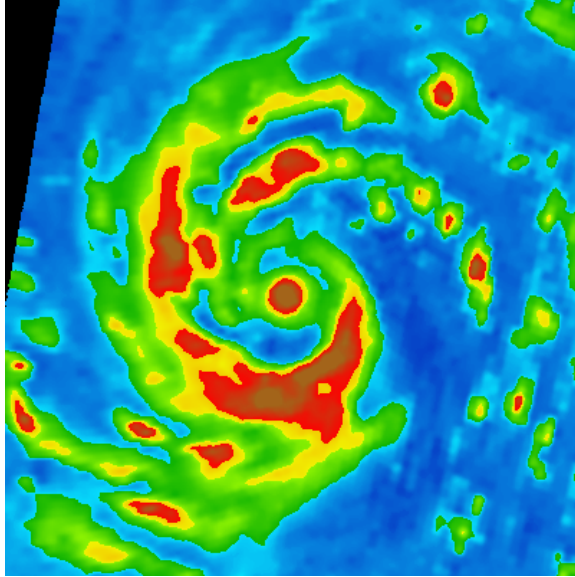| Original Dataset Total	80% and Land Restrictions	Missing Data Removed	Images within 1-hour Removed
15,164	1,869	1,645	1,496

Figure 14. Typhoon Phanfone (2014) - Example of an image that was missing a small amount of data, in the top left corner.

Finally, once all manual quality control was complete the images were binned according to the Dvorak T-number that most closely approximates their corresponding, interpolated best track intensity. The Dvorak T-number is known to represent unique structures within visible/IR imagery. Therefore, it follows that microwave imagery may also exhibit unique patterns within these bins. The number of images analyzed in each bin are listed in Table 5.

3.4 Cluster Analysis

Once the data was fully processed cluster analysis was applied to identify recurring patterns. Clustering is accomplished by providing pieces of information, or variables, about each object (images for this research) to the computer, which creates clusters based on a similarity measure. The variables supplied to the algorithm are

Table 5. The number of images in each Dvorak bin after all restrictions were applied.

Dvorak Number	T1	T2	T2.5	T3	T3.5	T4	T4.5	T5	T5.5
# of Images	319	144	156	181	136	114	99	124	80

user defined. Many different methods of creating variables were tested, since there was no previous research that set a standard approach. One method tested was dividing the image into sections of rings and quadrants and then taking the mean or sum of each section. However, the final approach chosen was dividing the image into octants and computing statistical measures on each section to form the variables. This method will be described in the following section.

3.4.1 Description of Cluster Analysis Variables

Initially, using rings of equal thickness as sections was contemplated. However, in order to focus on the inner area of the storm that drives the TC intensity, the thickness of the rings was varied based on the inner core and outer core definitions by Weatherford and Gray (1988). The inner core rings which occupy the region from 0-60 pixels radially from the center pixel, were 10 pixels thick. The outer core rings that were 61-140 pixels from the center were 20 pixels thick. Between 141-200 pixels from the center pixel there were two rings, each 30 pixels thick. The corners remaining after the final ring was created were considered one section, producing 13 different sections. Next, these rings were divided into octants resulting in the 104 sections shown in Figure 15.

One complication noted during previous variable testing was addressed for the final creation of variables. The pixel values of the blue T_B are higher than the pixel values of the red, yellow and green T_B, illustrated in Figure 12. The red and yellow pixels are important for the clustering solution, since they represent convection within the TC. When the only statistical measure used to cluster is the mean or sum of each section the higher blue pixels could mask convection in a section. Therefore, multiple statistical measures were employed to cluster the images based on the full spectrum of the pixels. The mean, median, maximum, minimum, standard deviation, and
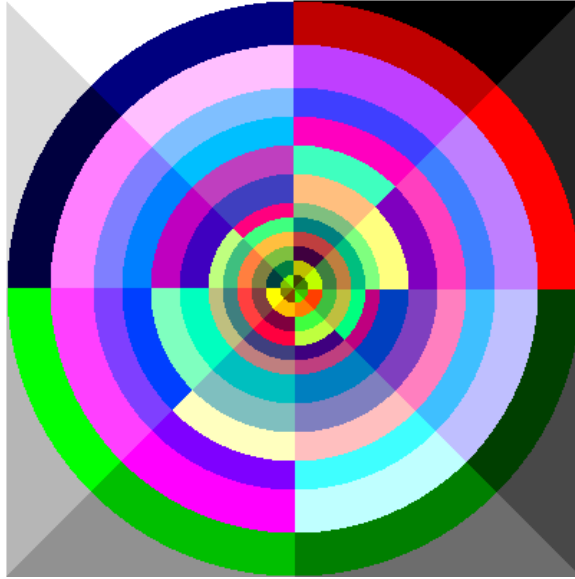
Figure 15. This figure illustrates the octants that each image was divided into, using the definitions of inner-core and outer-core by Weatherford and Gray (1988)

interquartile range were taken of each section and set as the variables, which resulted in 624 variables. These variables will be applied for use in two different clustering algorithms, hierarchical and k-means.

3.4.2 Hierarchical Clustering

There are three primary options within hierarchical clustering, which were described in Section 2.5. Three trials were conducted using hierarchical clustering for this research, the settings are displayed in Table 6. The linkage method and the approach used to cut the hierarchical tree, from now on referred to as the cut method, remained consistent throughout the trials The distance metric and number of maximum clusters (k) were varied.

Table 6. The settings chosen for each trial.

	Distance Metric	Linkage Method	Cut Method
Trial 1	Correlation	Complete	Max Clusters
Trial 2	Euclidean	Complete	Max Clusters
Trial 3	City Block	Complete	Max Clusters

Preliminary testing revealed that complete linkage was the best method for this dataset. Single linkage consistently produced multiple one-image clusters and one extensive cluster that contained the majority of the images, which were unsurprisingly highly dissimilar. Average linkage did not perform as poorly as single linkage but the images clustered together were less similar to the eye than with complete linkage. The cut method was set as maximum clusters instead of the inconsistency coefficient because this provided more control for determining the optimal number of clusters.

Three different ways to calculate the distance between two objects s and t are defined in Equations 2 - 4, where x_s and x_t represent vectors of n variables that describe each object such that $x_s = [x_{s1}, x_{s2}, ..., x_{sn}]$ and $x_t = [x_{t1}, x_{t2}, ..., x_{tn}]$. In Equation 2, $\bar{x}_s = \frac{1}{n} \sum_j x_{sj}$ and $\bar{x}_t = \frac{1}{n} \sum_j x_{tj}$. Additionally, the apostrophe indicates the result is the transpose of the vector calculated within the parentheses (The MathWorks Inc, 2015). The distance metric that subjectively performed the best in preliminary testing was the correlation distance. It is defined as one minus the sample correlation between points:

$$d_{st} = 1 - \frac{(x_s - \bar{x}_s)(x_t - \bar{x}_t)'}{\sqrt{(x_s - \bar{x}_s)(x_s - \bar{x}_s)'}\sqrt{(x_t - \bar{x}_t)(x_t - \bar{x}_t)'}}. \tag{2}$$

Next, for validation of the Trial 1 results, Trial 2 was completed with the Euclidean distance. This was chosen because it is the most common distance metric. The Euclidean distance is the distance between two objects if a straight line were drawn between them and is defined as:

$$d_{st}^2 = (x_s - x_t)(x_s - x_t)'. \tag{3}$$

Finally, for robustness a third trial was completed using the city block metric. The city block metric computes the distance as if the path between two objects could

only follow lines on a Cartesian coordinate system, similar to how city blocks are organized. There were only four distance metrics remaining that could be used both in hierarchical clustering and silhouette plots. The city block metric was the simplest remaining distance measure and is defined as:

$$d_{st} = \sum_{j=1}^{n} |x_{sj} - x_{tj}|. \tag{4}$$

The final piece of information required to run the cluster analysis was the number of maximum clusters (k). The optimal k was determined within each trial for individual intensity bins. The maximum clusters parameter was set at a minimum of two clusters and a maximum of $\frac{1}{3}$T, the total number of images per bin. Dendrograms and silhouette plots, introduced in Sections 2.5.2. and 2.5.3 respectively, were created for each of k = 2, 3, 4, ..., $\frac{1}{3}$T. The silhouette plots were examined starting with the highest k then stepping down. Potentially significant clusters were defined as clusters that were large relative to the others and contained members with highly positive silhouette values. These potentially significant clusters were identified as they appeared and were tracked through the process. When there was a step where a potentially significant cluster combined with another cluster and the intra-cluster similarity of the potentially significant cluster deteriorated the k directly prior to the merge was chosen. The dendrogram was used as a visualization tool to track which clusters combined on each step, Figure 16 illustrates this process.

In Figure 16 the left hand images each represent k=14, note clusters 3 and 5 in the top left silhouette plot. Cluster 5 was being tracked as a potentially significant cluster. The right hand images show the clusters formed when k=13. Referencing the dendrograms confirms that clusters 3 and 5 did combine to form a new cluster 3 that has many images with negative silhouette values. In this case the number of clusters was set at k=14 in order to retain cluster 5 as a significant cluster. Once
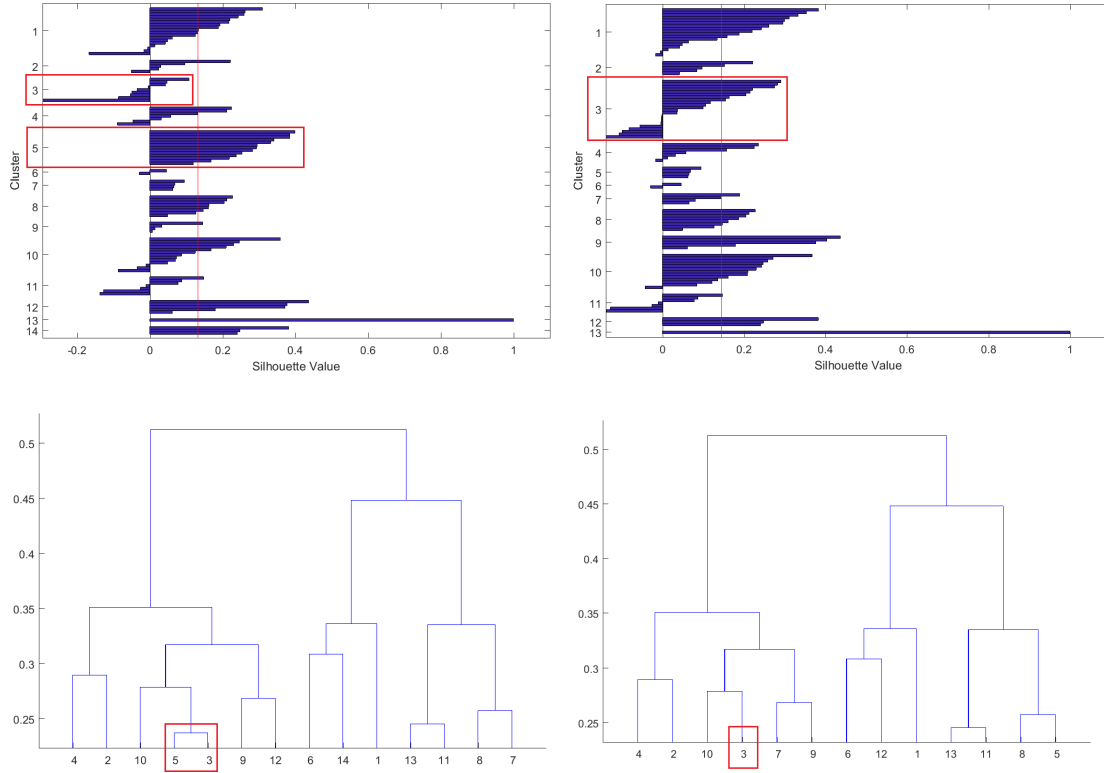
Figure 16. The method employed to determine the optimal value for k.

k was chosen the hierarchical cluster analysis was run. The next section details the options chosen for k-means cluster analysis.

3.4.3 K-means Clustering

Although k-means is the most simple clustering algorithm there are options within the MATLAB k-means function that result in more or less accurate results. Similar to hierarchical clustering, the user must decide which distance metric to instruct the function to use. For k-means the distance metric is used to compute the centroid of each cluster. K-means is used in this research as a secondary clustering technique. Therefore, only the correlation distance metric that was subjectively identified as the best option within hierarchical clustering is used. Secondly, within k-means you can set the maximum number of iterations the function can complete. The

36

maximum iterations was set at 100, which was more than enough as most instances converged within 10 iterations. The number of replications supplied is important information when using k-means clustering. As discussed in Section 2.5.3 there could be thousands of local optima for a dataset of only 200 objects with 8 variables (Steinley and Brusco, 2007). Since there is a maximum of 319 objects with 624 variables being clustered in this research the possible local optima is likely in the millions. However, due to computational restraints, 100,000 replications was set as the constraint.

K-means was actually the first clustering algorithm tested for this research and was applied to a subset of the data from 2016-2017. These initial results were promising but it was difficult to scale to the full dataset. The primary challenge was identifying the optimal k. The traditional "objective" methods of determining k such as the elbow method and built-in functions in MATLAB yielded inconsistent results. The suggested k was typically either two or the highest k that had been presented as a choice, which indicated that these methods were unable to reliably identify an acceptable k. Therefore, k-means was only applied after k was identified during the hierarchical clustering steps. Then, the same k determined in that step was applied to the k-means clustering. Not all of the clusters identified were significant though. The criteria used to differentiate between significant and insignificant clusters will be discussed in the following section.

3.4.4 Determining Significant Clusters

Two standards were set to identify significant clusters. First, the cluster had to contain at least 5% of the number of images within the intensity bin. The 5% threshold was subjectively chosen to eliminate clusters that only contained a few images but ensure that all clusters were not eliminated as most clusters contained less than 10% of the images within a bin. Secondly, the average silhouette value of

the cluster had to exceed the average silhouette value of the entire intensity bin. For example, referencing the top left panel in Figure 16 the average silhouette value for Cluster 5 is certainly higher than that of the entire bin, denoted by the red line.

The images from all significant clusters were then saved with the cluster number in the filename. All images with positive silhouette values within the cluster were composited to create a representative image for the cluster. The composites were created by taking the mean of each pixel value and assigning it to a new matrix then saving it with the original color map. Furthermore, the image with the highest silhouette value was also saved. Once all trials were completed and significant clusters selected the results were visually inspected to find significant patterns.

3.5 Significant Pattern Requirements

The significant clusters that met three final requirements were classified as significant patterns. First, the cluster could not contain more than three negative silhouette value images. However, if the cluster contained less than 13 images the negative silhouette images had to be less than a quarter of the total cluster. Secondly, the cluster had to contain images from at least three different storms. Finally, images within the cluster had to look reasonably similar to the cluster composite (Figure 17).
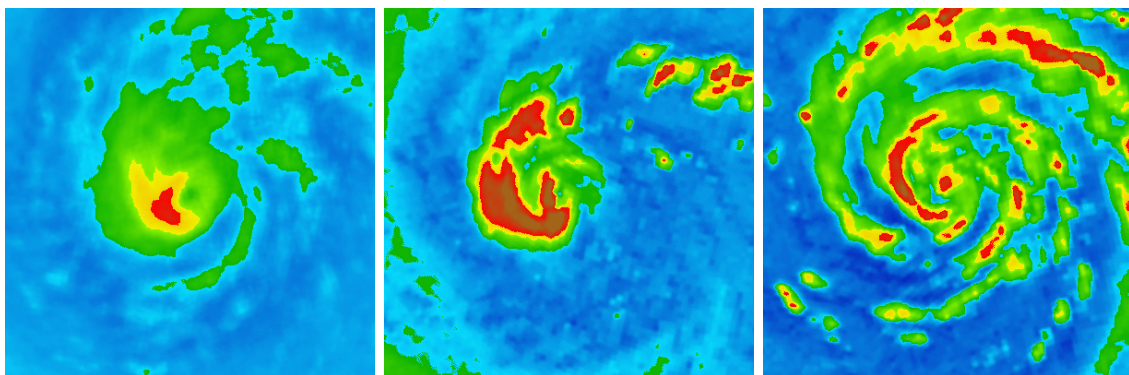
Figure 17. The composite image (left) with a reasonably similar image (middle) and a dissimilar image (right) all from a significant cluster that did not meet criteria to be classified as a significant pattern.
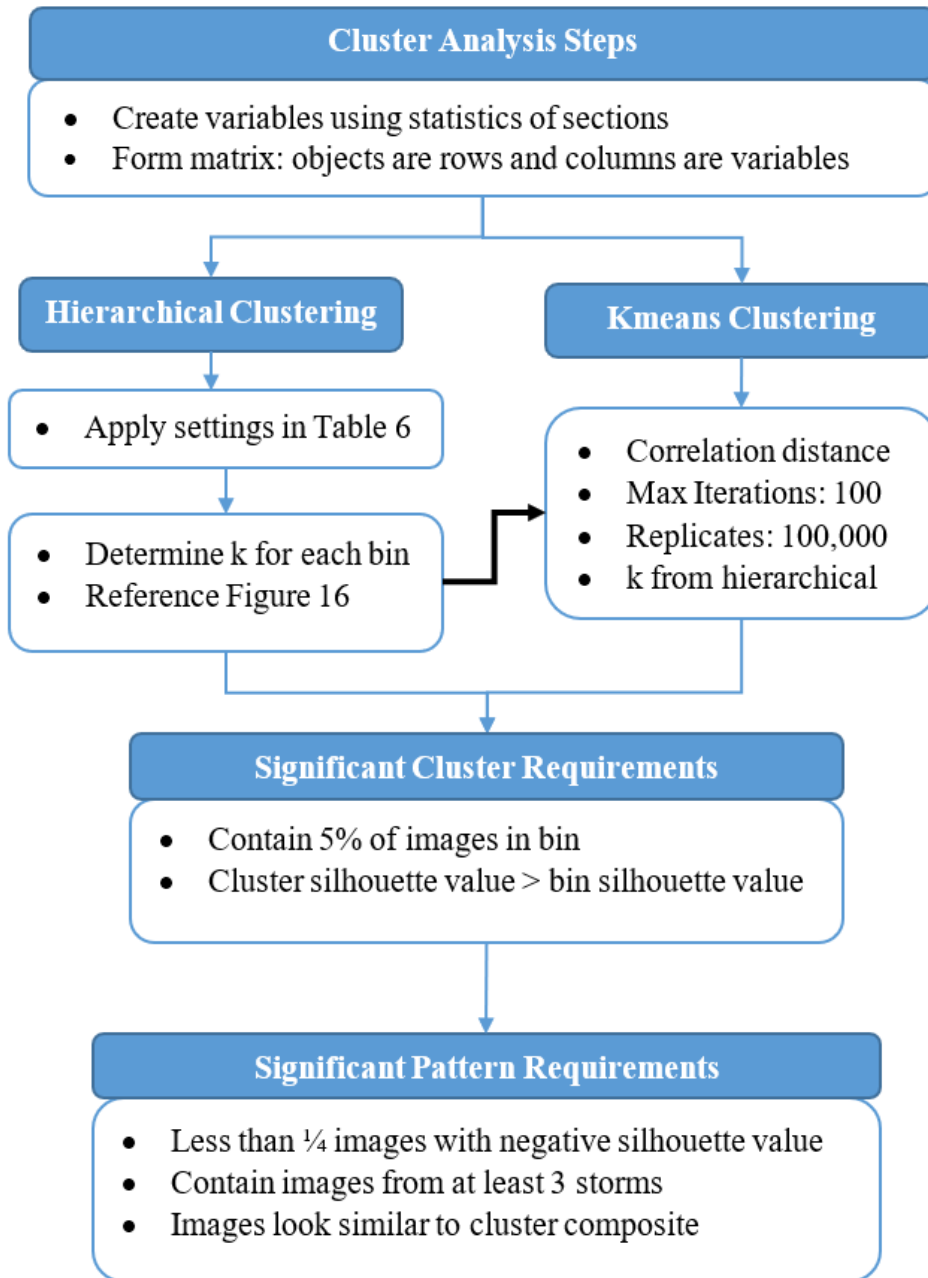
Figure 18. The cluster analysis process

Figure 18 condenses the steps followed to perform the cluster analysis into a simple flowchart. In the next chapter the results of the analysis using hierarchical and k-means clustering will be presented.

IV. Analysis and Results

Overview

The composite images from each significant cluster are presented and compared for the three hierarchical clustering trials. The data are displayed in two different manners. First, they are depicted numerically, both by the number of significant clusters per trial and the number of images within each significant cluster. Secondly, the composite images are displayed to allow visual evaluation of the results. The significant patterns that span all three trials are presented first as the most dominant patterns. Next, the significant clusters identified in each trial are shown separated by trial. Finally, a chart of all significant patterns that appeared in at least two trials is shown. Additionally, the k-means clustering results will be presented for comparison.

4.1 Numeric Results

Prior to performing the final cluster analysis k had to be determined, as described in Section 3.4.2. Table 7 displays the k values used for each intensity bin. Notice that k varies throughout each trial, sometimes drastically such as in T3.

Table 7. The values of k applied for hierarchical cluster analysis

	Trial 1	Trial 2	Trial 3
T1	72	40	59
T2	18	18	25
T2.5	21	27	29
T3	28	45	25
T3.5	15	19	24
T4	18	12	12
T4.5	11	20	18
T5	18	13	13
T5.5	8	11	12

Table 8. Columns 2-4 display the number of significant clusters that were initially identified during the clustering. Columns 5-7 show how many clusters were considered significant patterns once the restrictions in Section 3.5 were imposed. Numbers that changed are displayed in red in columns 5-7.

	# Significant Clusters			# Significant Patterns		
	Trial 1	Trial 2	Trial 3	Trial 1	Trial 2	Trial 3
T1	1	1	1	1	1	1
T2	2	1	1	2	1	1
T2.5	2	1	1	2	1	1
T3	2	0	2	2	0	2
T3.5	3	3	3	3	3	3
T4	4	5	4	4	4	4
T4.5	4	4	5	3	3	4
T5	1	5	4	0	4	4
T5.5	4	4	6	3	3	5

Once the significant clusters were identified they were scrutinized using the criteria described in Section 3.5. Table 8 shows how the number of clusters changed when the restrictions were applied, highlighted in red text. Trials 1 and 2 contained three and four significant clusters, respectively, that did not meet the significant pattern requirements. However, in Trial 3 there were only two significant clusters that were not able to be classified as significant patterns.

The number of images within each significant pattern is important when considering the legitimacy of a given pattern. Table 9 shows the total number of images in each intensity bin, the minimum cluster size (5% of image total), and the number of images per cluster for the significant patterns. Since the composites were created without the negative silhouette value images, the number of positive images are included in the right three columns with all changes are red. Finally, the colors represent similar patterns: green spans all three trials and yellow spans two trials.

Table 9. Total number of images in each intensity bin, the minimum cluster size (5% of image total), the number of images per significant pattern, and the number of positive silhouette value images per pattern. Differences between Columns 4-6 and Columns 7-9 are typed in red. The colors represent similar patterns: green spans all three trials and yellow spans two trials.

	Image Total	Minimum Cluster Size	Initial Clusters			Negative Values Removed		
			Trial 1	Trial 2	Trial 3	Trial 1	Trial 2	Trial 3
T1	319	16	39	56	40	39	55	38
T2	144	8	27	-	27	27	-	27
			19	20	-	18	20	-
T2.5	156	8	20	23	19	19	22	19
			26	-	-	24	-	-
T3	181	10	11	-	22	10	-	20
			20	-	17	18	-	17
T3.5	136	7	8	13	7	7	11	7
			9	8	7	9	8	7
			17	12	10	17	12	10
T4	114	6	10	25	26	9	22	23
			8	8	10	7	8	10
			7	8	8	6	8	8
			8	8	7	8	8	7
T4.5	99	5	22	6	12	20	6	12
			10	5	5	10	5	5
			9	8	9	9	8	9
			-	-	5	-	-	5
T5	124	7	-	10	12	-	9	10
			-	9	7	-	8	7
			-	15	12	-	15	11
			-	9	11	-	9	10
T5.5	80	4	10	8	7	10	7	6
			7	7	8	7	7	8
				5	7	-	5	7
			16	-	8	14	-	8
			-	-	5	-	-	5

4.2 Pattern Results

4.2.1 Hierarchical Clustering Results

There were seven patterns that spanned all three trials, shown in Figure 19. As the intensity increases the inner TC structure becomes more defined and the areas of convection are more pronounced. Note that while the patterns are similar there are some differences among different distance metrics. For instance, all of the T4.5 patterns are similar but not identical. This may indicate more robust results because different images were clustered that resulted in a similar composite image.

All significant clusters identified in Trials 1, 2, and 3 are displayed in Figures 20, 21, and 22 respectively. The T1 pattern was not included to allow the remaining images to be larger. The only T1 pattern identified is in Figure 19. When referencing an image within these figures they will be labeled as: Dvorak bin (column number) (e.g. T3.5(2)). The bold line separates significant patterns on the left from significant clusters that did not meet all pattern requirements. The significant patterns are further categorized by the number of trials they appeared in. The green border indicates that they occurred in all trials, yellow means 2 trials, and red means 1 trial. Lastly, the Saffir-Simpson scale is on the left for readers more familiar with that scale.
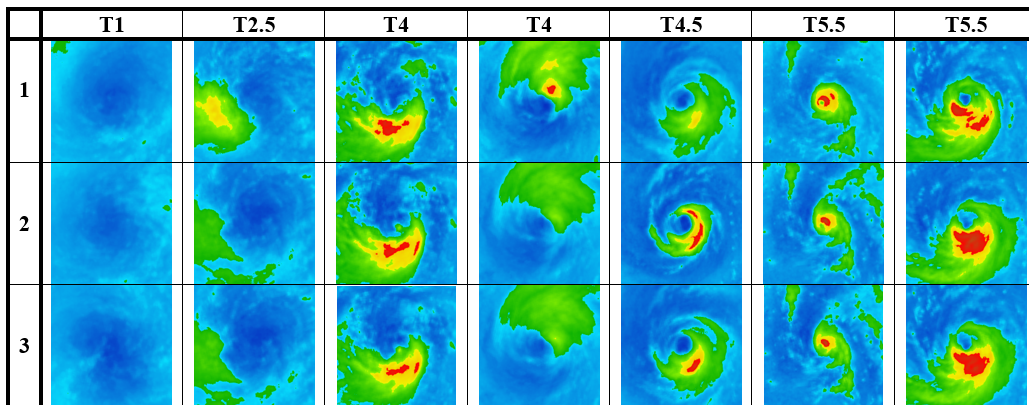

Figure 19. The significant patterns that spanned all three trials, the first column denotes the trial number.
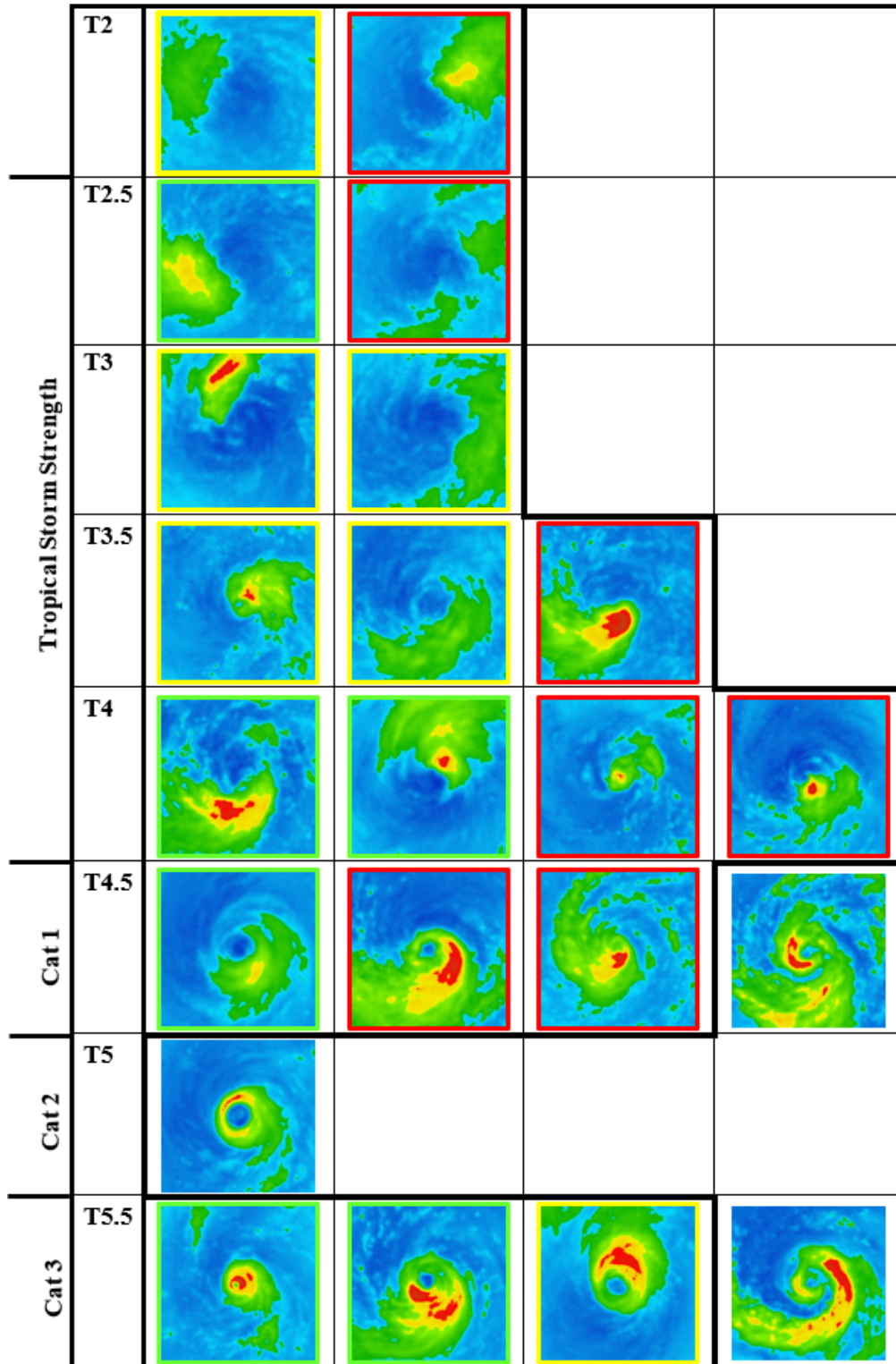
Figure 20. All significant clusters identified for Trial 1 from T2-T5.5. Images left of the bold line are significant patterns. The image border indicates how many times that pattern repeats: green appears in all 3 trials, yellow in 2, and red in 1. The left hand side displays approximate equivalent intensity in the US Saffir-Simpson Scale.

Figure 21. All significant clusters identified for Trial 2 from T2-T5.5. Images left of the bold line are significant patterns. The image border indicates how many times that pattern repeats: green appears in all 3 trials, yellow in 2, and red in 1. The left hand side displays approximate equivalent intensity in the US Saffir-Simpson Scale.
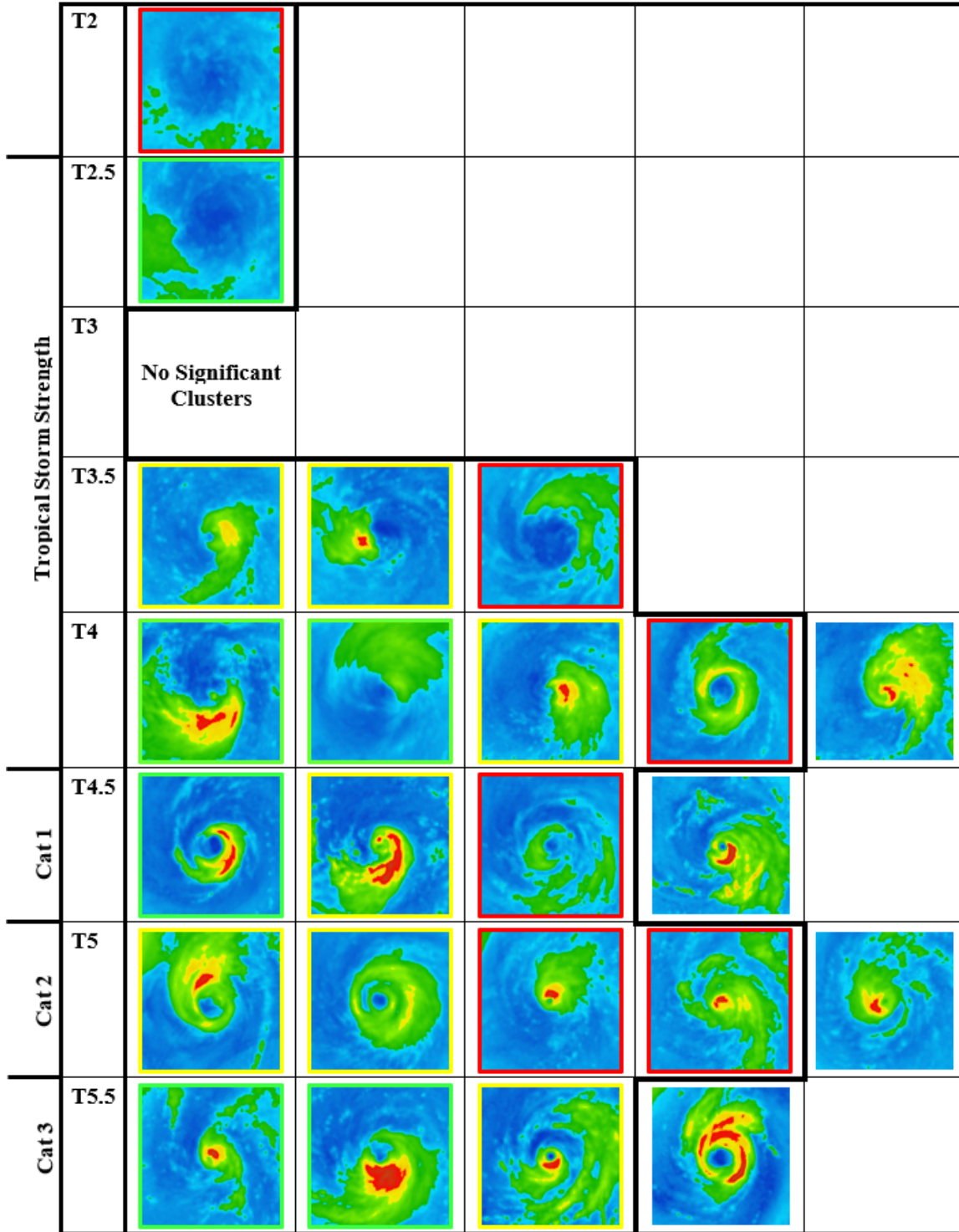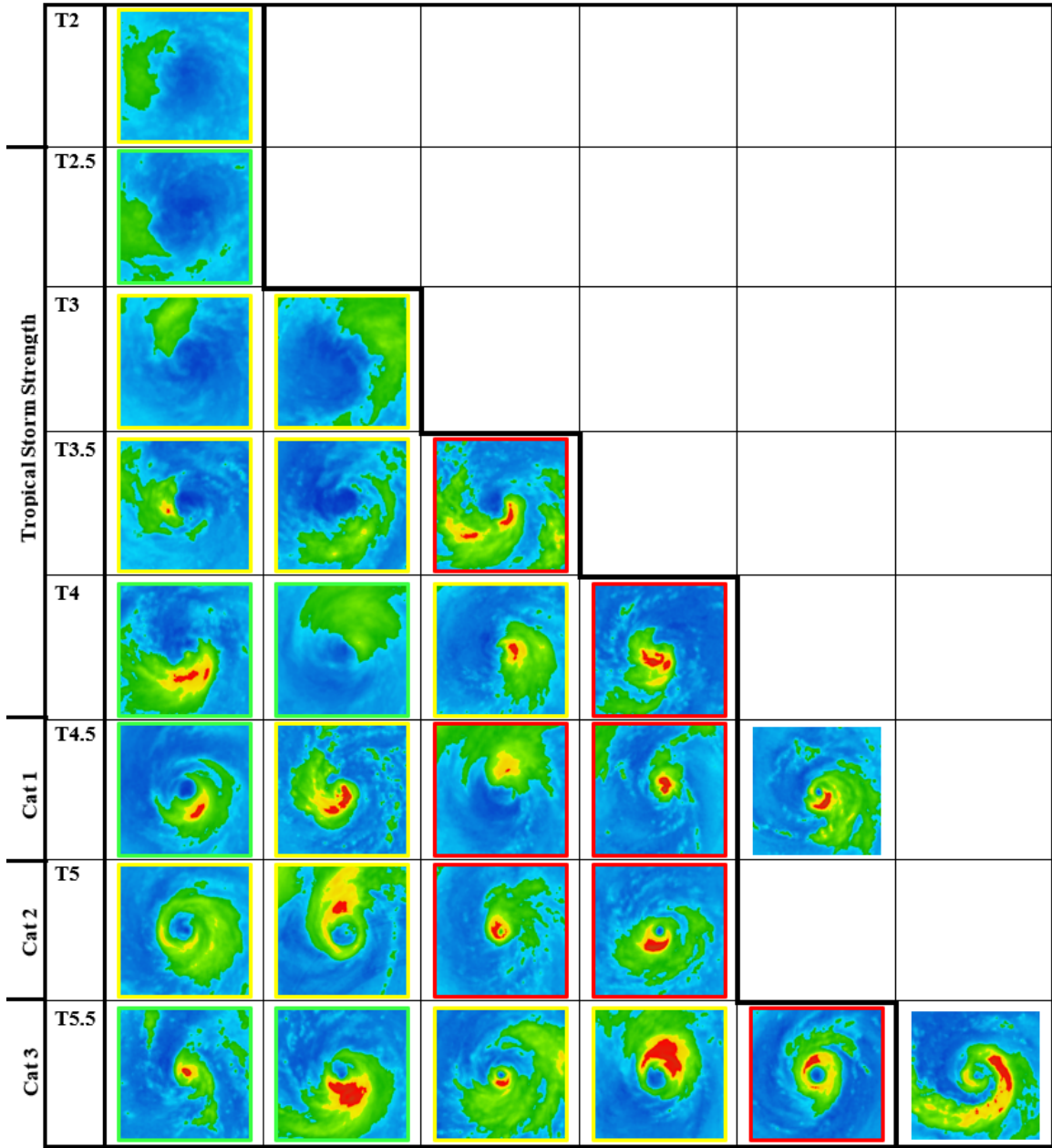
Figure 22. All significant clusters identified for Trial 3 from T2-T5.5. Images left of the bold line are significant patterns. The image border indicates how many times that pattern repeats: green appears in all 3 trials, yellow in 2, and red in 1. The left hand side displays approximate equivalent intensity in the US Saffir-Simpson Scale.

In Trial 1 23 significant clusters were identified and 20 met the requirements to be a significant pattern. Out of 20 significant patterns: 7 appeared in 3 trials, 6 in 2 trials, and 7 appeared in Trial 1 only. In Trial 2 there were 24 significant clusters

and 20 met the requirements to be classified as a significant pattern. Out of the 20 significant patterns: 7 appeared in 3 trials, 7 in 2 trials, and 6 appeared in Trial 2 only. In Trial 3 there were 27 significant clusters and 25 met the requirements to be a significant pattern. Out of the 25 significant patterns: 7 appeared in 3 trials, 11 in 2 trials, and 7 appeared in Trial 3 only.

Examining Figures 20, 21, and 22 reveals similar patterns that span multiple intensity bins. For example, in Figure 22 T3.5(3) and T4(1) display a similar structure; likewise, T5(3) and T5.5(1) in Figure 21 have comparable features. Additionally, there are patterns that would be very similar if rotated around an imaginary vertical axis at the TC center. For example T5(3), T5(4), and T5(5) in Figure 21 would resemble each other once rotated about the center. Similarly, in Figure 20 T5.5(2) and T5.5(3) would be alike once aligned. There are more comparisons that could be made in these figures, but this is a subjective analysis of the data where the results may be analyst dependent.

Finally, all significant patterns that appeared in at least two trials are displayed in Figure 23. The composites are displayed on the left and the image within each cluster with the highest silhouette value is shown on the right. The silhouette value is a measure of how likely an object is in the correct cluster. Therefore, the image with the highest silhouette value is proposed as most representative of the cluster. Figure 23 reveals that the composites represent the location of the convection well, but they do not always properly portray the intensity. Slight variations in the location of the strongest convection within each image in the cluster explains this. Red and yellow areas in the composites represent locations where convection was most consistent.

There are important caveats to note when viewing these results. Due to the limited images available for analysis in each bin some of these pattern are the result of only a few different storms or a hand-full of images. Specifically, clusters T4(1) and

T4(3) only contained images from 4 and 5 different storms, respectively. Additionally, clusters T4.5(2) and T5.5(4) were comprised of only 5 images in total. Finally, almost half of the images in cluster T5.5(2) are from the same storm. These specifics may vary slightly by trial, but are comparable to what has been listed for each pattern discussed.
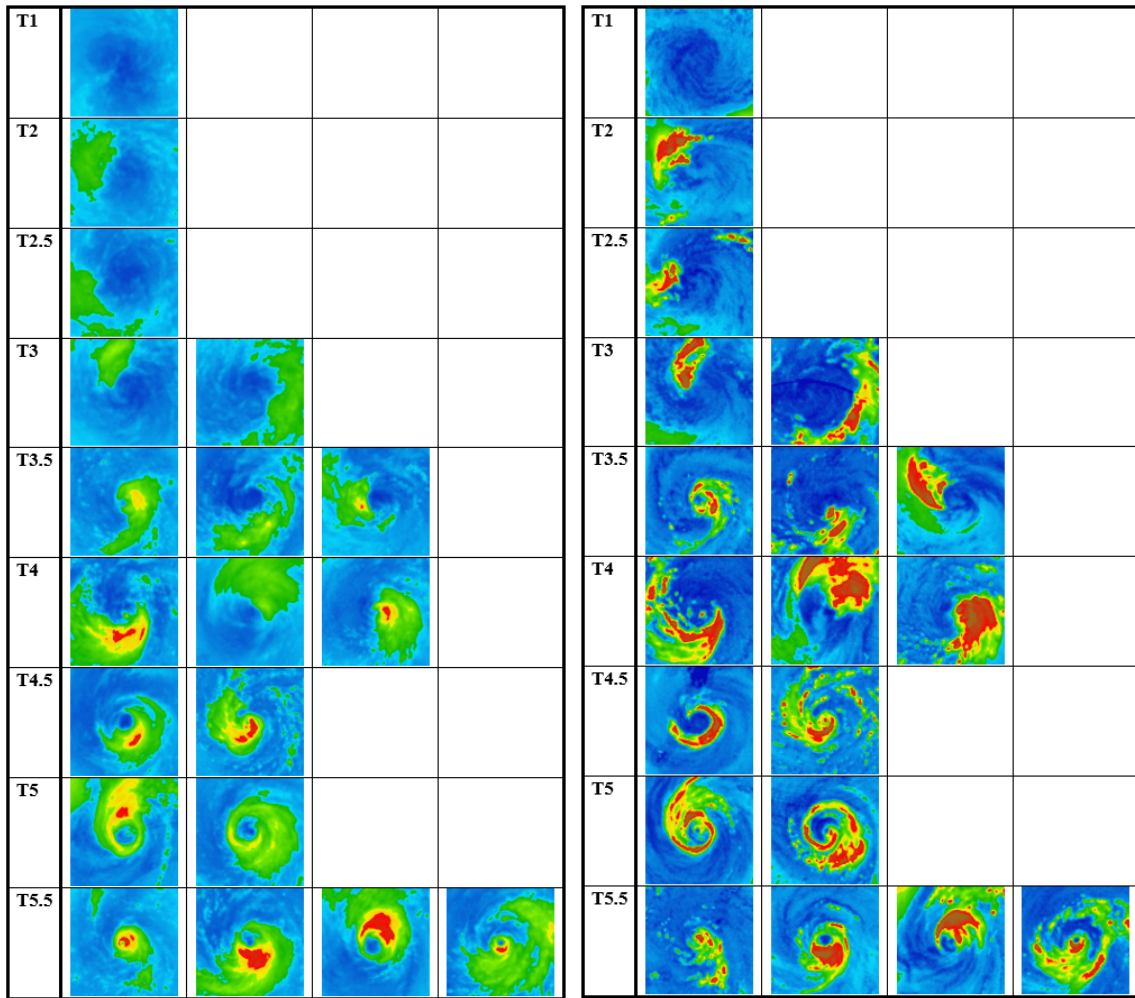

Figure 23. The significant patterns that spanned at least two trials. The composite images are on the left and the image with the highest silhouette value for that cluster is displayed on the right.

48

4.2.2 K-means Clustering Results

For comparison the same dataset was clustered using k-means with the k values listed in Table 7. Only Trial 1 was repeated due to time constraints on this research. Figure 24 contains the significant patterns determined by k-means cluster analysis. The T1 bin was not included because of the lack of patterns identified previously.

Figure 24 reveals similar patterns to those identified in Figure 23 as most robust by hierarchical cluster analysis. The images in Figure 24 that correspond to a pattern in Figure 23 are marked with an asterisk. Out of 23 significant patterns nine coincide with a pattern in Figure 23, which itself only contains 18 patterns between T2-T5.5. In general the patterns identified by k-means clustering show the same progression in TC structure with intensity. As the intensity increases the patterns become more defined with increased convection about the TC center.

4.2.3 Clustering Results using All Pixels

The method used to create the variables that produced the results up to this point was fairly arbitrary. The results may have changed if the rings were scaled differently or 16 sections were used instead of octants, for example. It is not feasible to test all possible variable configurations. However, clustering using individual pixels is a simplistic approach that removes the subjectivity of choosing sections.

The dataset was evaluated with hierarchical and k-means cluster analysis using each pixel as a variable, which resulted in 160,801 variables. The settings were kept the same as Trial 1 so results from the four different tests using the correlation distance metric could be compared. A new k was determined for each bin through the same methods described in Section 3.4.2, listed in Table 10. Furthermore, because the number of variables increased from 624 to 160,801 the k-means replications had to be adjusted. K-means replications were reduced from 100,000 to 1,000 due to limitations
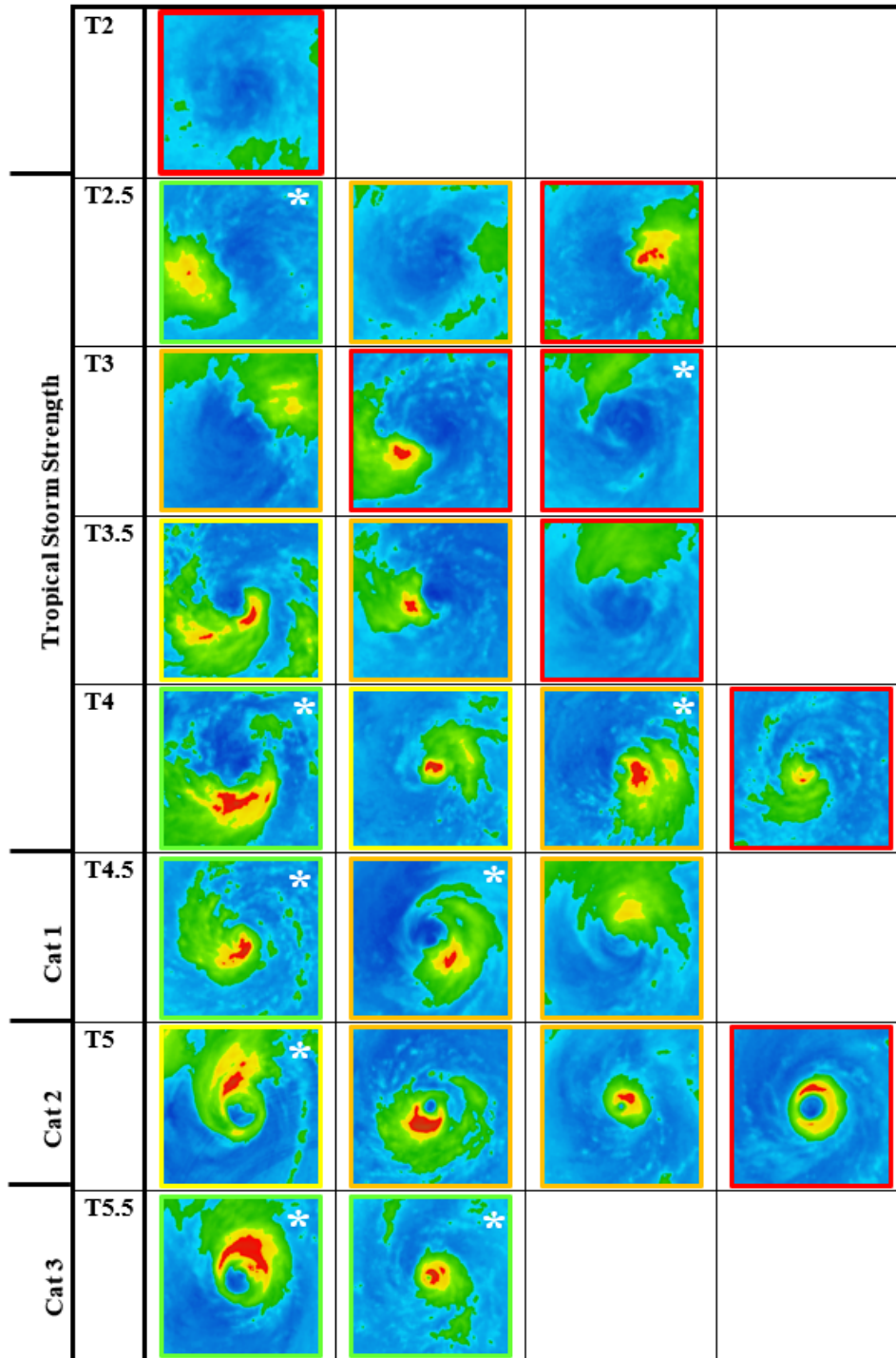
Figure 24. All significant patterns identified by k-means cluster analysis from T2-T5.5. The image border indicates how many times that pattern repeats within the tests using the correlation distance metric: green appears in all 4 tests, yellow in 3, orange in 2, and red in this test only. The left hand side displays approximate equivalent intensity in the US Saffir-Simpson Scale. The asterisks denote patterns that also appear in Figure 23.

Table 10. These are the values of k applied for both hierarchical and k-means cluster analysis when clustering by all pixels.

T1	T2	T2.5	T3	T3.5	T4	T4.5	T5	T5.5
26	30	13	19	16	13	11	11	11

in computing power.

The results of the hierarchical cluster analysis are presented in Figure 25 while Figure 26 displays results from the k-means cluster analysis. The image border indicates how many times that pattern repeats during the tests using the correlation distance metric: green appears in all four tests, yellow in three, orange in two, and red in only one. The significant patterns identified are similar to those pinpointed during the octant-variable trials. The TC structure again develops as would be expected with enhanced convection near the center at the intensity increases. There are no noticeable differences in the quality of clusters that are produced when the data are clustered using all of the pixels.

4.2.4 Analysis of Correlation Distance Results

Comparing the results from the four correlation distance tests provides interesting information. Figure 27 contains the significant patterns from the original Trial 1 in Section 4.2.1 with the borders adjusted to the new color scheme for comparison. The four tests resulted in a total of 94 significant patterns. Out of these 94 patterns 29 were selected in only one of the tests with 18 found in T2-T3.5 bins. Likewise, 30 spanned two tests meaning there were 15 unique patterns identified. Of these 15 patterns eight appeared between T2-T3.5 Additionally, 15 of these patterns were represented across three tests, meaning there were only five unique patterns. Of these five patterns that spanned three tests only one occurred between T2-T3.5. Finally, 20 covered all four tests constituting five unique patterns, only one of which was found between T2-T3.5. These five patterns are displayed in Figure 28.

51

Figure 25. All significant patterns identified by hierarchical cluster analysis from T2-T5.5, when clustering by all pixels. The image border indicates how many times that pattern repeats within the tests using the correlation distance metric: green appears in all 4 tests, yellow in 3, orange in 2, and red in this test only. The left hand side displays approximate equivalent intensity in the US Saffir-Simpson Scale.
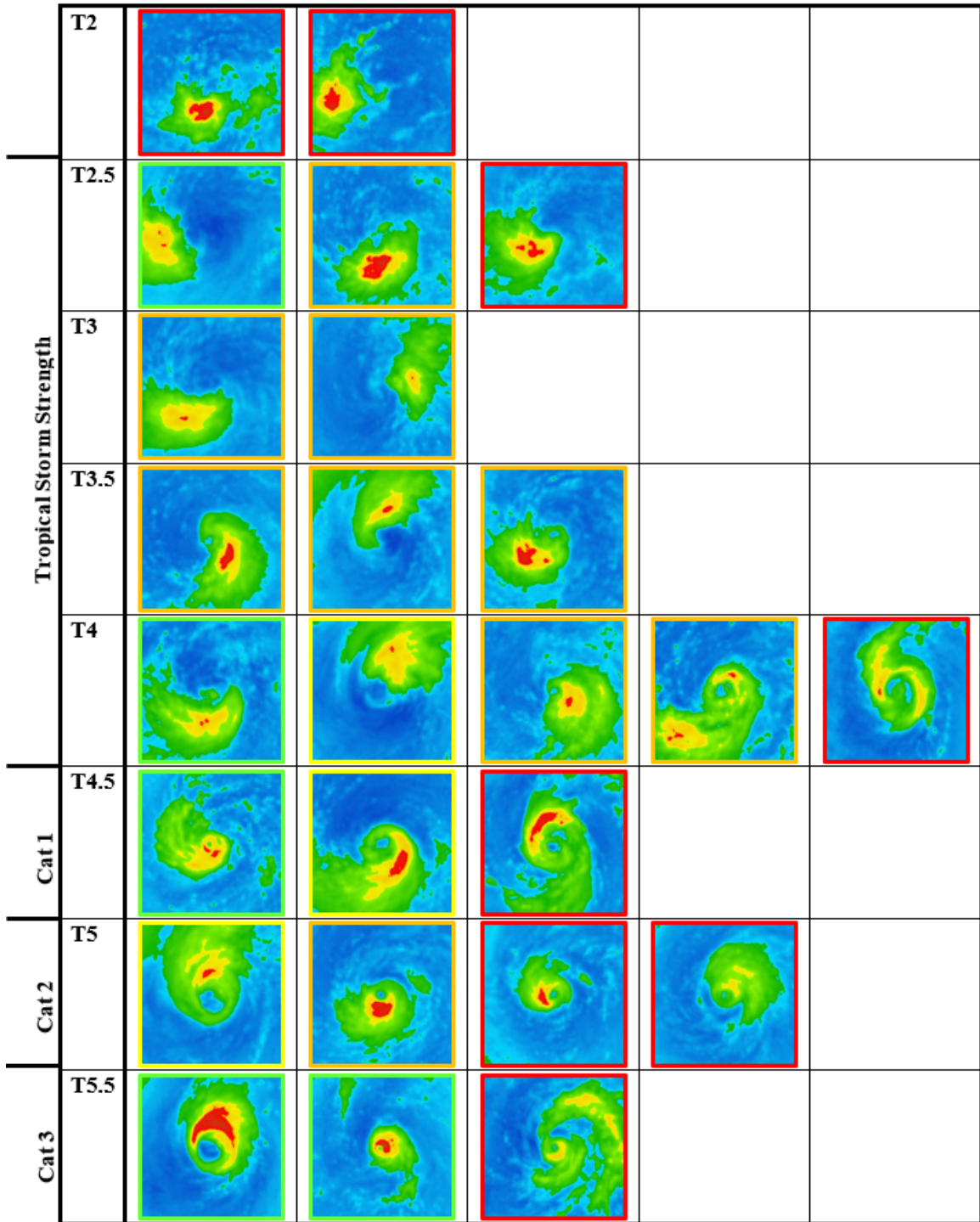
52
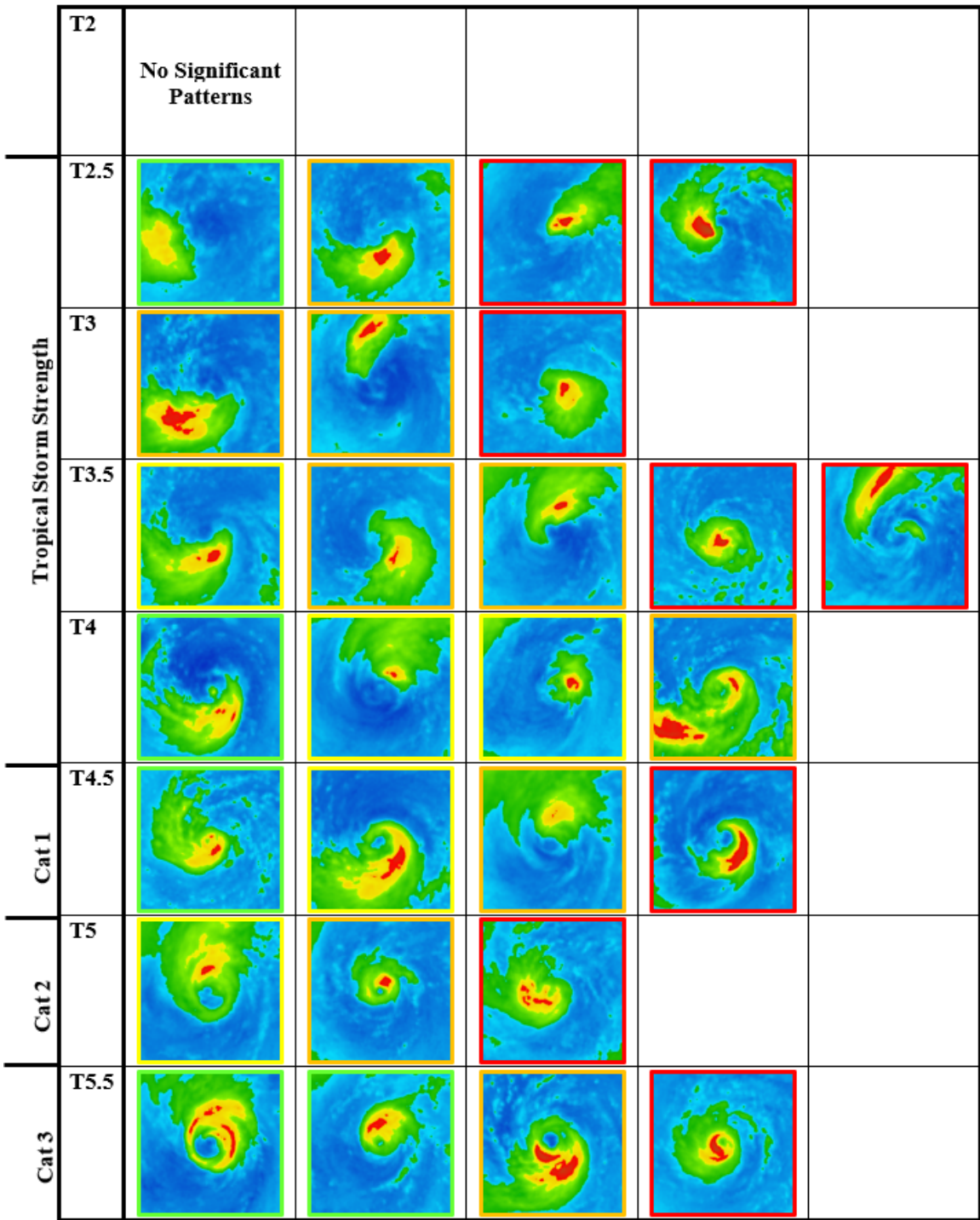
Figure 26. All significant patterns identified by k-means cluster analysis from T2-T5.5, when clustering by all pixels. The image border indicates how many times that pattern repeats within the tests using the correlation distance metric: green appears in all 4 tests, yellow in 3, orange in 2, and red in this test only. The left hand side displays approximate equivalent intensity in the US Saffir-Simpson Scale.

Figure 27. All significant patterns identified by hierarchical cluster analysis from T2-T5.5. These are the Trial 1 results with the image borders updated. The image border indicates how many times that pattern repeats within the tests using the correlation distance metric: green appears in all 4 tests, yellow in 3, orange in 2, and red in this test only. The left hand side displays approximate equivalent intensity in the US Saffir-Simpson Scale.
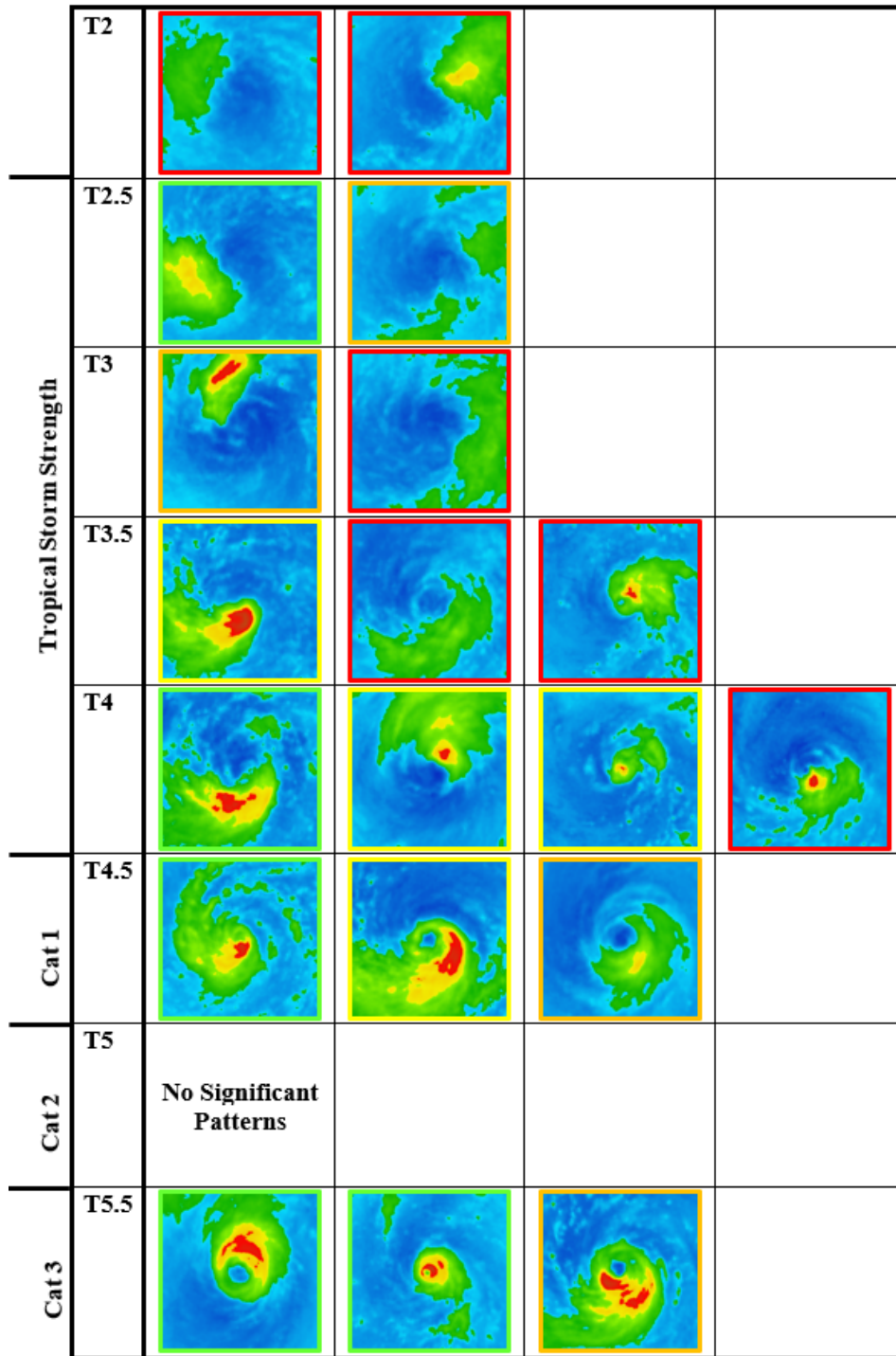
Further investigation of the patterns that appear in only two of the tests reveals an interesting result. Two tests were compared at a time where either the variable used was held constant or the clustering algorithm was the constant. Within each test the number of patterns that appeared in only two tests was identified. Next, the two were compared to determine how many two-test patterns they shared. For example, the two tests that used octant variable would be analyzed side by side. The number or two-test patterns would be noted for each test, then the number they had in common was recorded. This analysis was then conducted for the all pixels variable tests, k-means clustering, and hierarchical clustering also. Finally, pairs were compared where no parameter was held constant. So, the k-means all pixels result was compared to the hierarchical octant result and vice versa. Table 11 shows how many patterns coincided per pair with the number of patterns that could have been shared for each pair in the far right column.

There are seven similar patterns out of a possible 13 that could have been shared when the variable is held constant. In contrast, there are only two like patterns out of a possible twelve that could have been shared when the clustering technique is held constant. Furthermore, there are six similar patterns out of a possible twelve when neither parameter is held constant.

Table 11. The number of two-test patterns that coincide within each pair with the total number of patterns that could have been shared in the far right column. The left hand column identifies what parameter is being held constant.

Held Constant:	Description	Patterns that Coincide	Max Possible Patterns
Clustering Variables	Octants	2	4
	All Pixels	5	9
Clustering Technique	Hierarchical	0	4
	Kmeans	2	8
Mixed	Mixed 1	2	4
	Mixed 2	4	8

	T2.5	T4	T4.5	T5.5	T5.5
Composite					
Most Representative Image					
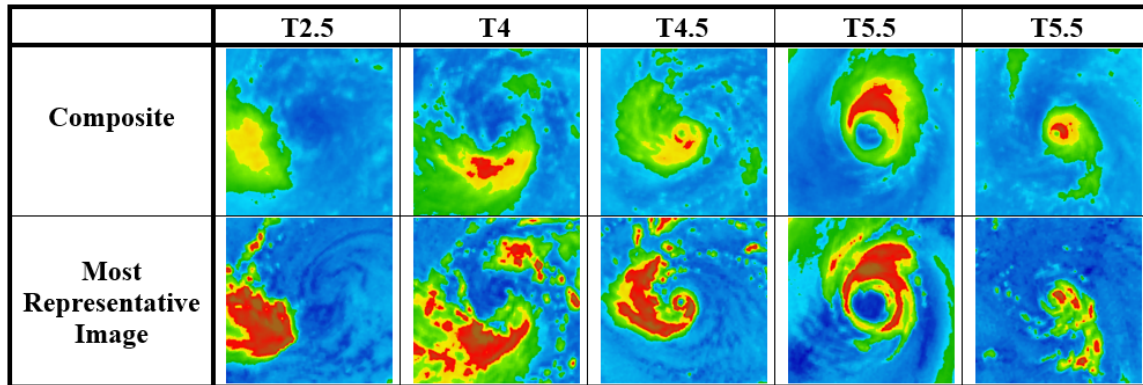
Figure 28. The significant pattern that spanned all four correlation distance tests. The top row is the composite image and the bottom is the highest silhouette value.

The five patterns that occurred in all four tests also coincide with patterns initially identified in Figure 23. However, there are some caveats on these patterns as the dataset was limited. The primary limitation was the total number of images within each cluster, with the exception of the cluster in T2.5. The remaining four patterns were crafted from clusters that had ten or less images in the cluster, which affects the legitimacy of the final pattern.

V. Discussion and Conclusions

5.1 Summary of Results

Cluster analysis was employed to analyze the data in lower intensity bins from T1-T5.5 and ascertain if there is a relationship between microwave patterns and TC intensity. First, hierarchical clustering was applied to the dataset with the clustering variables created by partitioning the images into 104 sections. Three trials were conducted for this portion of the analysis utilizing three different distance metrics, but keeping all other parameters constant. Figure 23 presented the patterns that appeared in at least two of the three trials as the most significant results from this portion of the research. The patterns identified match the expected TC structure at each given intensity. In the T1 bin the convection is sparse and disorganized to the point that only low clouds are visible in the composite. In bins T2-T3 the areas of enhancement are located in the outer core and image periphery, not in the TC center. Once the storms intensify to T3.5 the convection increases and begins to infiltrate the inner core. At T4 the spiral structure sets up with amplified convection near the center of the storm. The spiral structure with enhanced convection around the center escalates in the T4.5 bin and an eye takes form by T5 and T5.5. The TC development revealed by these results is a good indication of their validity.

The second set of results displayed used the correlation distance metric, but varied the clustering technique and variables. There were four tests completed using the correlation distance, two applied k-means and two hierarchical clustering. The number of times patterns repeated across trials was noted in Chapter IV. If the dataset is separated into lower intensity storms (T2-T3.5) and higher intensity storms (T4-T5.5) an interesting result emerges. Of the patterns that occur in only one test 18 of 29 are from the lower intensity bins. On the contrary, out of the 10 unique

patterns that emerged in at least three tests only two were in the lower intensity bins. This development supports that the more defined structure in the higher intensity bins lends itself to repeating patterns as opposed to the disorganized convection that characterizes the lower intensity bins.

Additionally, the second set of results reveals an interesting trait when the patterns that spanned two tests are examined. Table 11 shows number of two-test patterns that coincide within each pair defined. When the clustering variable is held constant the pairs share seven patterns out of a potential 13. In contrast, when the clustering technique is held constant only two of twelve possible patterns align. This may suggest that the data are more sensitive to the variables used to represent an object than the clustering technique applied. This is supported by a summary of cluster analysis by Jain (2010), which states that data representation is one of the more important factors impacting the performance of clustering algorithms. However, it is noteworthy that when neither parameter was held constant six of a possible twelve patterns aligned, which may indicate these initial findings are coincidental.

5.2 Limitations

There were four main categories of limiting factors that affected the final results of this study. First, there was limited data once all restrictions listed in Section 3.3 were imposed. The smallest intensity bin was T5.5, which contained 80 images. In general the bin size decreased as the intensity increased. Therefore, the number of images required to be considered a "significant cluster" also decreased, as it was set at 5% of the total bin size. Most significant clusters identified above T4 contained 10 images or less, which is a very small sample size. Additionally, the imagery was not divided into intensifying and decaying storms, which may affect the TC structure at a given intensity.

Secondly, there are multiple limitations specific to cluster analysis. The variables used were arbitrary and as discussed in the previous section may have an important role in the resulting patterns. Additionally, the initial distance metric applied, correlation, was chosen based on preliminary testing that showed it performed best when viewing the clusters in a silhouette plot. This was decided early in the research and the method used to make this determination was not purely objective. However, applying three different distance metrics was an effort to combat this limitation and reveal patterns that occurred across multiple trials. Furthermore, complete linkage was utilized because it provided the most distinct clusters. Although single linkage was determined to definitely be a bad choice for this research, average linkage may be feasible with more testing.

Thirdly, within cluster analysis there were limitations specific to k-means. K-means randomly places centroids so the resulting clusters can change with each replication, particularly when using such a high number of variables. To combat this k-means was replicated 100,000 times when clustering by octants and 1,000 when clustering by all pixels. However, this is the brute force method and is still not enough replications to determine the optimal answer as there could be millions of local optima (Steinley, 2003). Therefore, the k-means results presented are the best solution with the time constraints and computing power available.

Finally, possibly the most critical limiting factor to this research was how k was determined. Depending on the k that is used the significant clusters identified through the cluster analysis change because they are based on the silhouette values. As clusters join together they may fall below the average silhouette value of the entire bin or rise above it. Therefore, the result can be different with a different k. The analysis was completed many times varying the configurations and the final results presented appeared across multiple trials. This is again an attempt to offset the effect

of this limitation. Lastly, this is only one study completed on one basin with a small set of data. The research would need to be reproduced and built upon to validate all results presented here.

5.3 Future Work

5.3.1 Intensity Range

One result noted in Chapter IV was that similar patterns appeared across multiple intensity bins. Applying the same methodology across a range of intensity bins could allow patterns to be labeled with a wind speed range. For instance, T1-T3 could be run together to see if there were any common patterns. From there T2-T3.5, T2.5-T4, T3-T4.5, etc could also be analyzed.

To test the potential of this application all images in bins T4-T5.5 were subjected to the same methodology outlined in Chapter III. Hierarchical clustering, octant variables, and settings from Trial 1 laid out in Table 6 were used for this analysis. There were 417 images in the T4-T5.5 bins. When determining k there were two different values for k that seemed probable. First, when k=53 there were a number of large, highly positive clusters so these results are presented in Figure 29. Similarly, when k=15 there were well-defined clusters, these results are presented in Figure 30. Both figures contain patterns that repeated often during the individual runs presented in Chapter IV. Furthermore, the clusters found when k=15 are similar to those when k=53. The clusters chosen when k=15 are less detailed since they contain more images within each bin there is a higher likelihood of convection in different areas. It is important to note that these clusters were not quality controlled as described in Section 3.4.4 due to time constraints. However, this technique shows promise for identifying the intensity range of certain patterns.
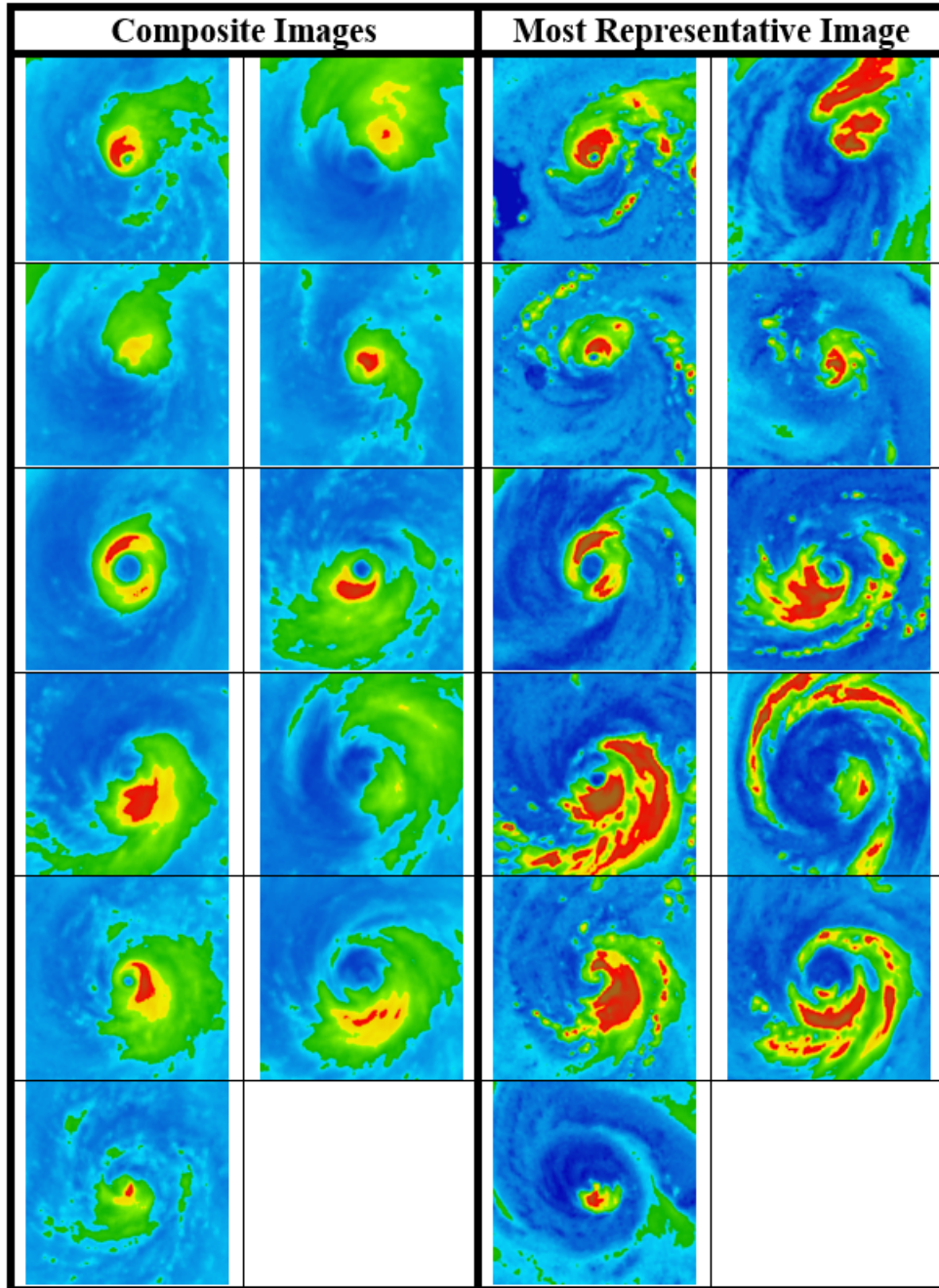
Figure 29. The clusters identified when applying hierarchical cluster analysis to the T4-T5.5 bins when k=53
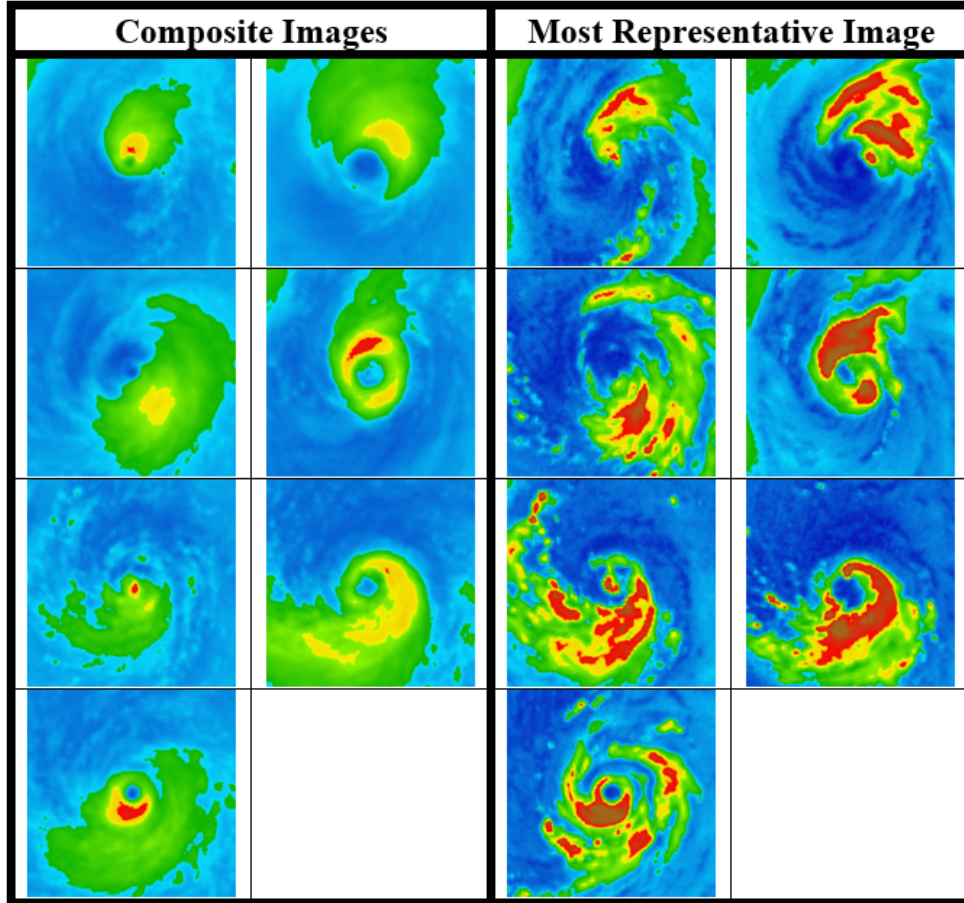
Figure 30. **The clusters identified when applying hierarchical cluster analysis to the T4-T5.5 bins when k=15**

5.3.2 JTWC Patterns

JTWC has a binder of microwave imagery patterns that are related to intensity, determined through empirical observations. Expanding this research to discover a pattern's intensity range, as described in the previous section, could be used to validate these patterns. The patterns that appeared in all four correlation distance tests displayed in Figure 28 are compared to images from the JTWC binder for any similarities.

Making comparisons between patterns is a subjective process, but there are a number of patterns that seem to relate to patterns in the JTWC binder. Figure 31

compares the T4 pattern in Figure 28 to a pattern called the "claw". The maximum sustained winds for the T4 bin is 65kts, which falls within the intensity range identified by JTWC. Furthermore, the T4.5 pattern resembles the "6s or 9s" pattern identified by JTWC compared in Figure 32. The T4.5 maximum sustained winds are 77kts which falls within the range determined by JTWC. These examples show that the results of this research support established empirically derived patterns.
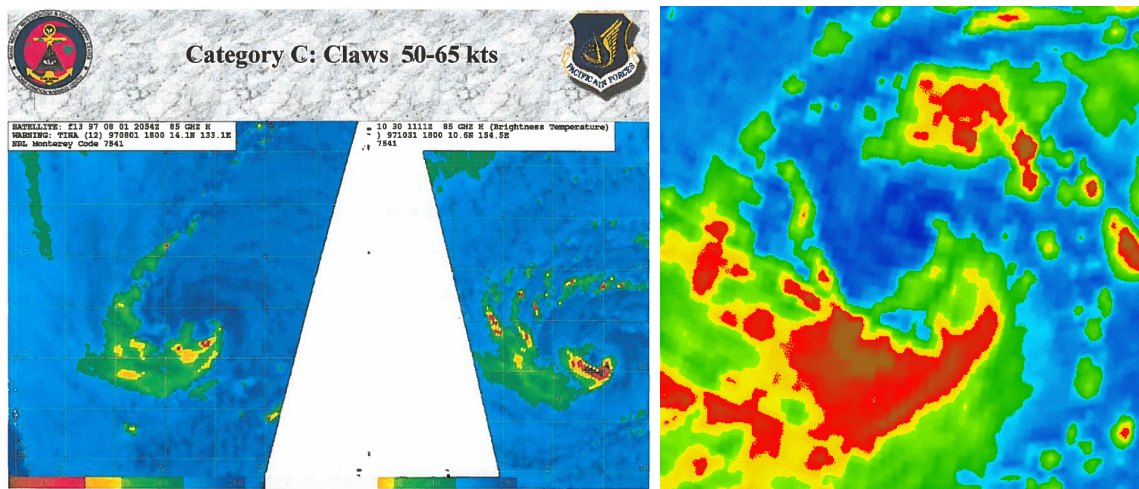

Figure 31. A "claw" microwave pattern compared to T4 pattern from Figure 28. Image on the left from Joint Typhoon Warning Center (2018).
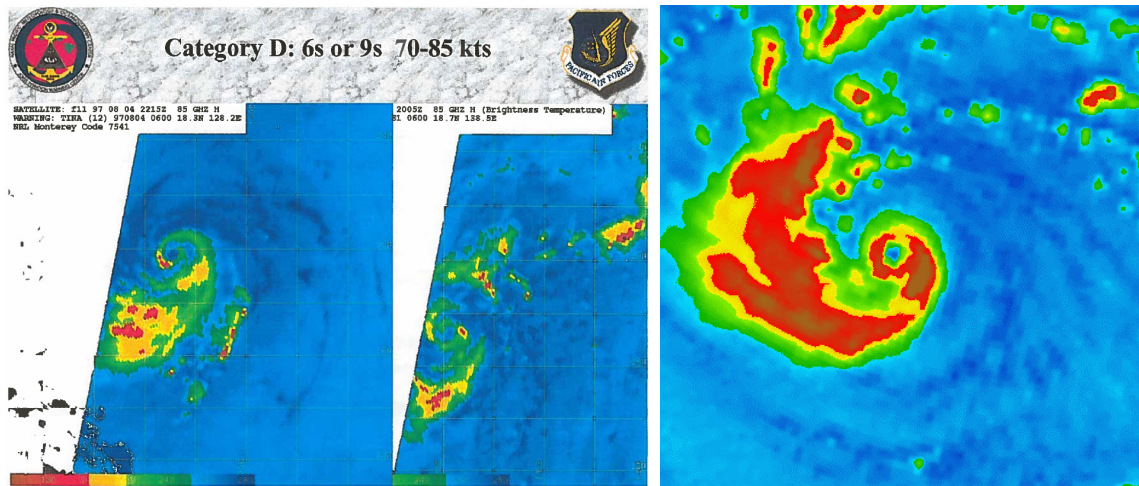

Figure 32. A "6s or 9s" microwave pattern compared to T4.5 pattern from Figure 28. Image on the left from Joint Typhoon Warning Center (2018).

5.3.3 Additional Future Work

One key limiting factor of this research was the amount of images analyzed. There are multiple ways this could be addressed in future studies. First, including images with missing data would greatly expand the dataset. However, different methods would need to be applied to use missing data in a clustering algorithm. Secondly, the analysis could be expanded to include other basins, which would increase the total number of images. Thirdly, other microwave imagers could be incorporated into the research. However, they would need to be normalized to the same T_B scale, which was outside the scope of this research. It is feasible though, Wimmers and Velden (2007) outlines how this was accomplished for the MIMIC product. Additionally, NRL has worked towards recalibrating all ice-scattering channels to 89 GHz to reduce this bias between sensors, which could be another avenue if these images become publicly available (Cossuth, 2017).

Cluster analysis specific advancements could focus on the variables used to cluster and a method for identifying the optimal clustering variables. Also, average linkage could be used instead of complete linkage. Additionally, determining the best placement for centroids when initializing k-means could drastically improve the ability to identify the optimal clusters. Furthermore, utilizing deep learning and convolutional neural networks to detect these patterns could greatly improve the results of this research and would allow the use of partial images..

Another avenue would be to use a similar methodology on TCs that are making landfall to see how interacting with land affects the structure of the TC, as revealed by microwave imagery. Additionally, some TCs could have radar imagery associated with their landfall that could be used to fill gaps in the microwave imagery.

Once microwave patterns that relate to intensity have been identified the next step could be to develop a pattern recognition technique similar to the Dvorak

Pattern-T method. Once developed this method could be tested by satellite analysts at JTWC and other TC centers to assess its effectiveness.

5.4 Conclusions

The objective of this thesis was to determine if there are patterns in microwave imagery that are related to TC intensity. Current intensity estimation techniques struggle at lower TC intensities, typically below 90 kts. Accurately representing the intensity of a TC is important for the forecast of a TC. The goal of JTWC is to provide accurate information on TCs in the Pacific and Indian Oceans so the US DoD can protect their assets and personnel in these areas.

While the results of this research are preliminary and require validation, they are promising. Multiple parameters were adjusted during this research to detect how these changes would affect the clustering solution to increase confidence in the final result. During the study two clustering techniques, three distance metrics, and two methods of creating the clustering variables were tested. Techniques similar to this could be used to validate the patterns subjectively identified by JTWC analysts. This would bolster the number of techniques available to assess TC intensity and possibly contribute to improved forecasts to protect DoD assets.

Appendix A
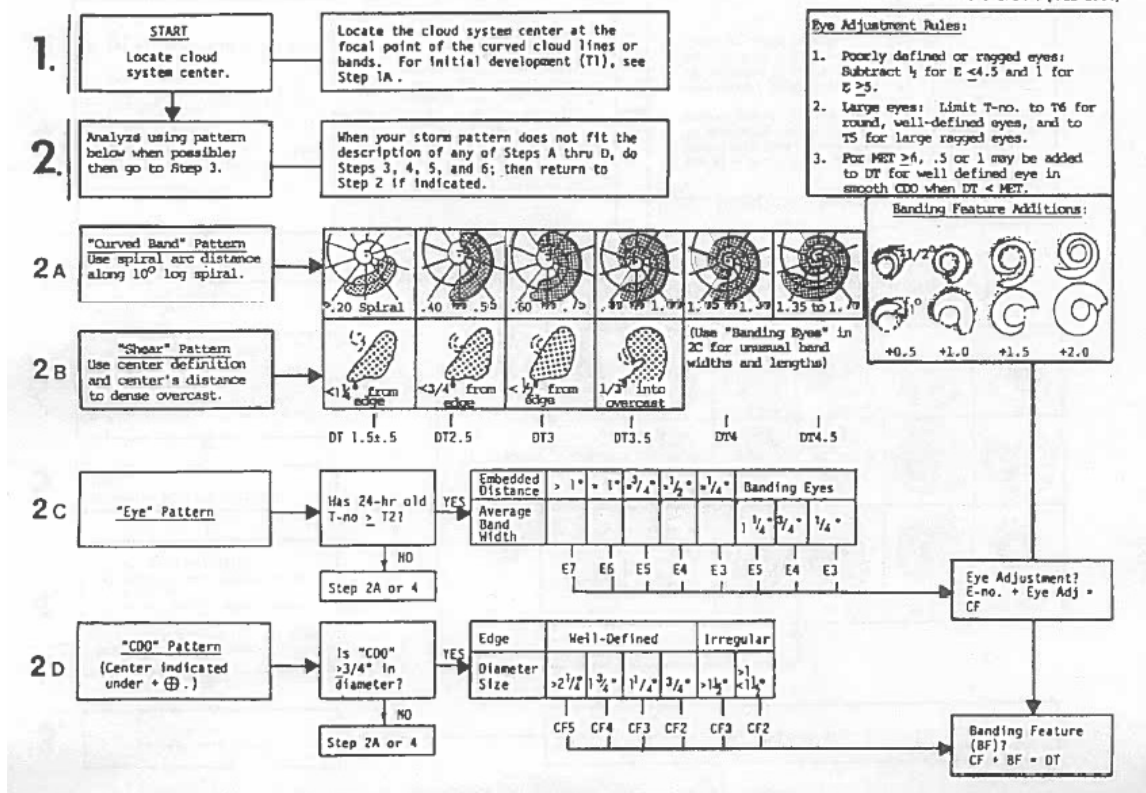
Figure 33. Part 1 of the detailed flow chart to determine intensity using visible imagery (Dvorak, 1984).

66

3. "Central Cold (Dense) Cover" Pattern

Rules: When past T-no. ≤T3, maintain model trend for 12 hours; then hold same. When past T-no. ≥T3.5 hold T-no. same. Use as final T-no.; then go to Step 9.

4. Determine past 24-hour trend. Is Development, Weakening, or Same indicated in a change of:
(a) center or eye characteristics, or
(b) center's involvement with dense overcast.

5. Determine Model Expected T-no. (MET).

6. Determine pattern T-no. Select pattern in diagram that best matches your storm picture within one column of the MET. Adjust MET .5 when indicated.

| PT 1.5 ±.5 | PT 2.5 | PT 3.5 | PT 4 | PT 5 | PT 6 |

a. CURVED BAND TYPE

b. CDO TYPE — 1° · 1¼° · 1¾° · 2½° · 1°

c.

When cloud comma is extremely small (<2½° lat), subtract 1 from pattern number.

7. T-no. Determination:
1. Use data T-no. from Step 2 when cloud features are clear-cut.
2. Use Pattern T-no. when DT is not clear and adjustment to MET is made.
3. For all other cases, use the MET.

8. Final T-number Constraints:
1. Initial classification must be T1 or T1.5.
2. During first 48 hours of development, T-no. cannot be lowered at night.
3. 24 hrs after initial T1, storm's T-no. must be <T2.5.
4. Final T-no. limits: <T4: change of 1/2 over 6 hrs. >T4: change of 1 over 6 hrs, 1.5 over 12 hrs, 2 over 18 hrs, and 2.5 over 24 hrs.
5. Final T-no. must = MET ±1.

9. Current Intensity (CI) Number Rules:
1. Use CI = final T-no. except when final T-no. shows change to weakening trend, or when redevelopment is indicated.
2. For initial weakening, hold CI same for 12 hours, then hold CI ½ or 1 higher than T-no. as storm weakens.

10. 24-Hr Forecast:
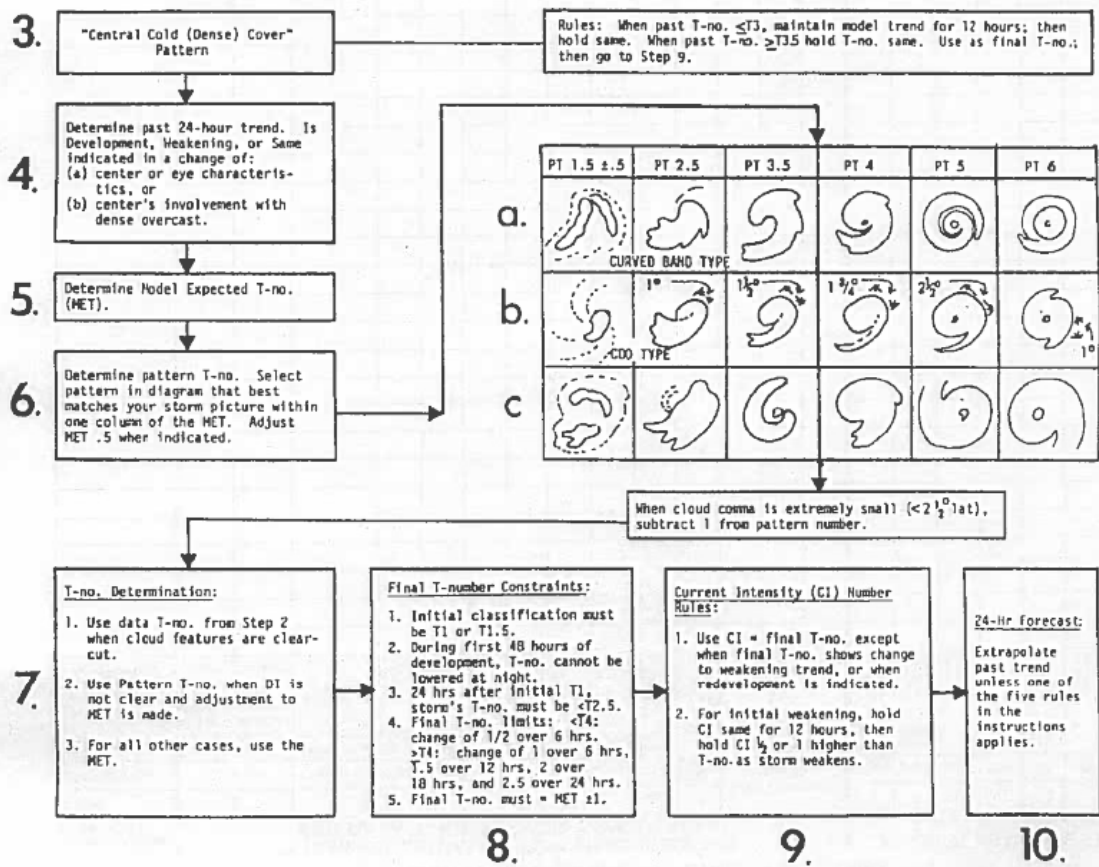Extrapolate past trend unless one of the five rules in the instructions applies.

Figure 34. Part 2 of the detailed flow chart to determine intensity using visible imagery (Dvorak, 1984).

Bibliography

Bankert, R. L. and Cossuth, J. H. (2016). Tropical Cyclone Intensity Estimation via Passive Microwave Data Features. In *AMS 32nd Conference on Hurricanes and Tropical Meteorology*.

Blake, E. S., Landsea, C. W., and Gibney, E. J. (2011). The Deadliest, Costliest, and Most Intense United States Tropical Cyclones from 1851 to 2010 (and other frequently requested hurricane facts). Technical Report NOAA Technical Memorandum NWS NHC-6. `https://www.nhc.noaa.gov/pdf/nws-nhc-6.pdf`.

Blumenfeld, J. (2015). From TRMM to GPM: The Evolution of NASA Precipitation Data. `https://earthdata.nasa.gov/trmm-to-gpm`.

Cecil, D. J. and Zipser, E. J. (1999). Relationships between Tropical Cyclone Intensity and Satellite-Based Indicators of Inner Core Convection: 85-GHz Ice-Scattering Signature and Lightning. *Monthly Weather Review*, 127(1):103–123.

Chan, J. C. L. and Kepert, J. D. (2010). *Global Perspectives on Tropical Cyclones*, volume 4 of *World Scientific Series on Asia-Pacific Weather and Climate*. WORLD SCIENTIFIC.

CIMSS (2019). CIMSS SATCON. `http://tropic.ssec.wisc.edu/misc/satcon/info.html`.

Cossuth, J. H. (2017). Passive Microwave Data Exploitation via the NRL Tropical Cyclone Webpage. Technical report, Naval Research Laboratory. Available at: `https://www.nhc.noaa.gov/jht/15-17reports/Cossuth_MOU_progress_report4_092917.pdf`.

Daloz, A. S., Camargo, S. J., Kossin, J. P., Emanuel, K., Horn, M., Jonas, J. A., Kim, D., Larow, T., Lim, Y. K., Patricola, C. M., Roberts, M., Scoccimarro, E., Shaevitz, D., Vidale, P. L., Wang, H., Wehner, M., and Zhao, M. (2015). Cluster analysis of downscaled and explicitly simulated North Atlantic tropical cyclone tracks. *Journal of Climate*, 28(4):1333–1361.

Du, J., Kimball, J. S., Shi, J., Jones, L. A., Wu, S., Sun, R., and Yang, H. (2014). Inter-calibration of satellite passive microwave land observations from AMSR-E and AMSR2 using overlapping FY3B-MWRI sensor measurements. *Remote Sensing*, 6(9):8594–8616.

Dvorak, V. (1984). Tropical Cyclone Intensity Analysis Using Satellite Data. Technical report, NOAA, Washington, D.C. Available at `https://satepsanone.nesdis.noaa.gov/pub/Publications/Tropical/Dvorak_1984.pdf`.

Gorbunov, M. E. and Kutuza, B. G. (2018). Cosmos-243 as the Starting Point for the Development of Microwave Radiometry Methods of the Earths Atmosphere and Surface. *Izvestiya, Atmospheric and Oceanic Physics*, 54(3):275–281.

Gray, W. M. (1968). Global View of the Origin of Tropical Disturbances and Storms. *Monthly Weather Review*, 96(10):669–700.

Hawkins, J. D., Member, A., Turk, F. J., Lee, T. F., Richardson, K., and Member, A. (2008). Observations of Tropical Cyclones With the SSMIS.pdf. *IEEE Transactions on Geoscience and Remote Sensing*, 46(4):901–912.

Herndon, D. C. and Velden, C. S. (2016). Estimation of Tropical Cyclone Intensity Using the CIMSS ATMS Tropical Cyclone Intensity Algorithm. In *21st Conference on Satellite Meteorology*. Available at: `https://ams.confex.com/ams/21SATMET20ASI/webprogram/Paper297022.html`.

Hollinger, J. P. (1990). DMSP Special Sensor Microwave/Imager Calibration/Validation Final Report Volume I. Technical report, Naval Research Laboratory, Washington, D.C.

Hou, A. Y., Kakar, R. K., Neeck, S., Azarbarzin, A. A., Kummerow, C. D., Kojima, M., Oki, R., Nakamura, K., and Iguchi, T. (2014). The global precipitation measurement mission. *Bulletin of the American Meteorological Society*, 95(5):701–722.

Hurricane Research Division (2014). Frequently Asked Questions. `http://www.aoml.noaa.gov/hrd/tcfaq/F1.html`.

Jain, A. K. (2010). Data clustering: 50 years beyond K-means. *Pattern Recognition Letters*, 31(8):651–666.

Joint Typhoon Warning Center (2018). Microwave Imagery Intensity Examples Binder. Unpublished manuscript.

Kidder, S. (1978). Estimating tropical cyclone central pressure and outer winds from satellite microwave data. *Mon. Wea. Rev.*, 106:1458–1464.

Kim, H. K. and Seo, K. H. (2016). Cluster analysis of tropical cyclone tracks over the western North Pacific using a self-organizing map. *Journal of Climate*, 29(10):3731–3751.

Kunkee, D. B., Poe, G. A., Boucher, D. J., Swadley, S. D., Hong, Y., Wessel, J. E., and Uliana, E. A. (2008). Design and evaluation of the first special sensor microwave imager/sounder. *IEEE Transactions on Geoscience and Remote Sensing*, 46(4):863–883.

Lee, T. F., Turk, F. J., and Hawkins, J. D. (2002). Interpretation of TRMM TMI Images of Tropical Cyclones. *Earth Interactions*, 6(3):1–17.

NASA. GPM Core Observatory. `https://pmm.nasa.gov/GPM/flight-project/core-observatory`. Retrieved on 21 December 2018.

NASA. TRMM Instruments. `https://pmm.nasa.gov/TRMM/trmm-instruments`. Retrieved on 21 December 2018.

Olander, T. L. and Velden, C. S. (2007). The Advanced Dvorak Technique: Continued Development of an Objective Scheme to Estimate Tropical Cyclone Intensity Using Geostationary Infrared Satellite Imagery. *Weather and Forecasting*, 22(2):287–298.

Perkins, M. (2018). Methodology to Analyze Tropical Cyclone Intensity from Microwave Imagery. M.S. Thesis, Available at: `https://apps.dtic.mil/dtic/tr/fulltext/u2/1056264.pdf`.

Petty, G. W. (2006). *A First Course in Atmospheric Radiation*. Sundog Publishing, 2nd edition.

Pradhan, R., Aygun, R. S., Maskey, M., Ramachandran, R., and Cecil, D. J. (2018). Tropical Cyclone Intensity Estimation Using a Deep Convolutional Neural Network. *IEEE Transactions on Image Processing*, 27(2):692–702.

Ramsay, H. A., Camargo, S. J., and Kim, D. (2012). Cluster analysis of tropical cyclone tracks in the Southern Hemisphere. *Climate Dynamics*, 39(3):897–917.

Ritchie, L., Wu, C.-c., and Herndon, D. (2014). 8th International Workshop on Tropical Cyclones Topic 2 . 3 Objective Tropical Cyclone Intensity Analysis. (November 2016).

Rousseeuw, P. J. (1987). Silhouettes: A graphical aid to the interpretation and validation of cluster analysis. *Journal of Computational and Applied Mathematics*, 20(5):53–65.

Sakuragi, T., Hoshino, S., and Kitabatake, N. (2014). Development and verification of a tropical cyclone intensity estimation method reflecting the variety of TRMM/TMI brightness temperature distribution. Technical report, JMA.

Steinley, D. (2003). Local Optima in K-means Clustering: What You Dont Know May Hurt You. *Psychological Methods*, 8(3):294–304.

Steinley, D. and Brusco, M. J. (2007). Initializing K-means batch clustering: A critical evaluation of several techniques. *Journal of Classification*, 24(1):99–121.

Stenger, R. A. (2013). *Assessment of Tropical Cyclone Structure Variability*. PhD thesis, Naval Postgraduate School.

The MathWorks Inc (2015). Statistics and Machine Learning Toolbox. *User ' s Guide R 2015 a*, page 7916.

Tibshirani, R., Walther, G., and Hastie, T. (2001). Estimating the number of clusters in a data set via the gap statistic. *Journal of the Royal Statistical Society: Series B (Statistical Methodology)*, 63(2):411–423.

Velden, C. S. and Herndon, D. (2014). An Update on the SATellite CONsensus (SAT-CON) Algorithm for Estimating Tropical Cyclone Intensity. In *31st Conference on Hurricanes and Tropical Meteorology*.

Weatherford, C. L. and Gray, W. M. (1988). Typhoon Structure as Revealed by Aircraft Reconnaissance. Part I: Data Analysis and Climatology. *Monthly Weather Review*, 116:10321043.

Wimmers, A. J. and Velden, C. S. (2007). MIMIC: A New Approach to Visualizing Satellite Microwave Imagery of Tropical Cyclones. *Bulletin of the American Meteorological Society*, 88(8):1187–1196.

Wimmers, A. J. and Velden, C. S. (2010). Objectively determining the rotational center of tropical cyclones in passive microwave satellite imagery. *Journal of Applied Meteorology and Climatology*, 49(9):2013–2034.

Wimmers, A. J. and Velden, C. S. (2016). Advancements in objective multisatellite tropical cyclone center fixing. *Journal of Applied Meteorology and Climatology*, 55(1):197–212.

World Meteorological Organization (2017). *Global Guide to Tropical Cyclone Forecasting*.

REPORT DOCUMENTATION PAGE

Form Approved
OMB No. 0704–0188

1. REPORT DATE *(DD–MM–YYYY)*	2. REPORT TYPE	3. DATES COVERED *(From — To)*
21–02–2019	Master's Thesis	Oct 2017 — Mar 2019

4. TITLE AND SUBTITLE

CHARACTERIZATION OF TROPICAL CYCLONE
INTENSITY USING MICROWAVE IMAGERY

5a. CONTRACT NUMBER

5b. GRANT NUMBER

5c. PROGRAM ELEMENT NUMBER

6. AUTHOR(S)

Nelson, Amanda Mundell, Capt, USAF

5d. PROJECT NUMBER

5e. TASK NUMBER

5f. WORK UNIT NUMBER

7. PERFORMING ORGANIZATION NAME(S) AND ADDRESS(ES)

Air Force Institute of Technology
Graduate School of Engineering and Management (AFIT/EN)
2950 Hobson Way
WPAFB OH 45433-7765

8. PERFORMING ORGANIZATION REPORT NUMBER

AFIT-ENP-MS-19-M-087

9. SPONSORING / MONITORING AGENCY NAME(S) AND ADDRESS(ES)

Joint Typhoon Warning Center
Attn: Robert Falvey 425 Luapele Road
Pearl Harbor, HI 96860-3130
COMM 808-474-3946 FAX 808-471-5676
Email: robert.falvey.1@us.af.mil

10. SPONSOR/MONITOR'S ACRONYM(S)

JTWC

11. SPONSOR/MONITOR'S REPORT NUMBER(S)

12. DISTRIBUTION / AVAILABILITY STATEMENT

DISTRIBUTION STATEMENT A:
APPROVED FOR PUBLIC RELEASE; DISTRIBUTION UNLIMITED.

13. SUPPLEMENTARY NOTES

14. ABSTRACT

In the absence of wind speed data from aircraft reconnaissance of tropical cyclones (TCs), analysts rely on remote sensing tools to estimate TC intensity. For over 40 years, the Dvorak technique has been applied to estimate intensity using visible and infrared (IR) satellite imagery, but its accuracy is sometimes limited when the radiative effects of high clouds obscure the TC convective structure below. Microwave imagery highlights areas of precipitation and deep convection revealing different patterns than visible and IR imagery. This study explores application of machine learning algorithms to identify patterns in microwave imagery to infer storm intensity, particularly focusing on weaker storms where other analysis methods struggle. An analysis of 91 GHz Special Sensor Microwave Imager/Sensor imagery onboard various Defense Meteorological Satellite Program assets from February 2006 to 2017 is presented. Incorporating pattern recognition methods into the current analysis process at the Joint Typhoon Warning Center has the potential to significantly improve TC intensity estimates across all basins of responsibility.

15. SUBJECT TERMS

Microwave Imagery, Cluster Analysis, Tropical Cyclone, Intensity Estimation, Machine Learning

16. SECURITY CLASSIFICATION OF:			17. LIMITATION OF ABSTRACT	18. NUMBER OF PAGES	19a. NAME OF RESPONSIBLE PERSON
a. REPORT	b. ABSTRACT	c. THIS PAGE			Maj Omar Nava, AFIT/ENP
U	U	U	U	88	**19b. TELEPHONE NUMBER** *(include area code)* (937) 255-3636, x4518; Omar.Nava@afit.edu

Standard Form 298 (Rev. 8–98)
Prescribed by ANSI Std. Z39.18